On the Origin of Orphan Tremors & Intraplate Seismicity in Western Africa

Tolulope Morayo Olugboji[1,1,1], Yingping Lu[1,1,1], Adekunle Abraham Adepelumi[2,2,2], Folarin Kolawole[3,3,3], and Manoochehr Shirzaei[4,4]

[1]University of Rochester
[2]OAU, Ife, Nigeria
[3]University of Oklahoma
[4]Virginia Tech

January 6, 2024

Abstract

On September 5-7, 2018, a series of tremors were reported in Nigeria's capital city, Abuja. These events followed a growing list of tremors felt in the stable intra-plate region, where earthquakes are not expected. Here, we review available seismological, geological, and geodetic data that may shed light on the origin of these tremors. First, we investigate the seismic records for parent location of the orphan tremors using a technique suitable when a single-seismic station is available such as the Western Africa region, which has a sparse seismic network. We find no evidence of the reported tremors within the seismic record of Western Africa. Next, we consider the possibility of a local amplification of earthquakes from regional tectonics, reactivation of local basement fractures by far-field tectonic stresses, landward continuation of oceanic fracture zones, or induced earthquakes triggered by groundwater extraction. Our assessments pose important implications for understanding Western Africa's intraplate seismicity and its potential connection to tectonic inheritance, active regional tectonics, and anthropogenic stress perturbation.

Supporting Information for

On the Origin of Orphan Tremors & Intraplate Seismicity in West Africa

Olugboji, T. [1,*], Manoochehr Shirzaei[2],Yingping Lu.[1,2*], Adepelumi, A.A.[3] , Kolawole, F.[4]

[1] *Department of Earth and Environmental Sciences, University of Rochester, NY* [2] *Goergen Institute for Data Science, University of Rochester, NY* [3] *Department of Geology, OAU, Ife, Nigeria* [4] *School of Geology and Geophysics, University of Oklahoma, Oklahoma*

Contents of this file

Supplementary Tables 1, 2, and 3 (3 Tables) Supplementary Figures 1, 2, 3, 4ab, 5abcd (9 Figures)

Additional Supporting Information (File uploaded separately)

Captions for Datasets S1

Introduction

Benchmarks of the algorithm (**supplementary figures 1-3**) are presented using example events (**supplementary Tables 1**) and with trigger parameters (**supplementary table 2**) and properties (**supplementary table 3**). We provide supporting information showing extended analysis e.g., **supplementary figure 4a** shows all other anomalous cases in **supplementary table 1** (similar to Figure

4). **Supplementary figure 5a-d** is a scan for events in the tremor sequence. We present the manual digitization of the google earth image of Figure 6 in Dataset S1.

Benchmark of Single Station Detector

$$\Delta^0_{s-e}(^\circ)$$

$$\Delta^0_{s-e}(\mathrm{km})$$

When estimating the station-earthquake distance from the *P-SV* delay time, we extract dominant body wave phases by applying a high-pass filter (> 0.1 Hz) and using the ak135 1-D model (Kennett et al., 1995) implemented using the taup tool of (Crotwell et al., 1999). A first-order approximation for teleseismic distances, , or local/regional events,

can be used as a quick check for most detections (Havskov & Ottemöller, 2010):

$$\Delta s-e$$

$$t_s - t_{pp} < t_s - t_p$$

When the true epicentral distance is greater than 90 degrees, the core diffracted, *Pdiff* phase might be hard to detect, especially for low-magnitude events. In this case, the *PP* phase is often the clearest arrival and can be wrongly identified as the first arriving body wave, leading to an under-estimated

(since). We identify and correct for this error by using the differential time between the doubly reflected *SS* and the Rayleigh wave as a second check on the estimated distance. Vertically polarized shear-waves at large epicentral distances will travel at mid-lower mantle velocities ˜7 km/s and compared with typical Rayleigh wave group velocity ˜3.5 km/s provides a second approximation for the epicentral distance:

With the epicentral distance estimated from the pair of body waves or body-and surface waves, the next step is to estimate the arrival azimuth of the event. This is easily done using either the P-wave or the Rayleigh wave. We choose to use the Rayleigh wave in this study because of their larger amplitudes. To ensure the resistance of surface wave detection to false triggers: (1) we apply a band-pass filter for improving surface wave signal to noise ratio (0.006-0.2 Hz (Ekström, 2006)), and (2) we scan a time window where surface wave are expected to arrive:

$$\phi_{s-e} = \phi(t_{SW})$$

$$t_{SW} > t_P + \Delta_{s-e}/3.5$$

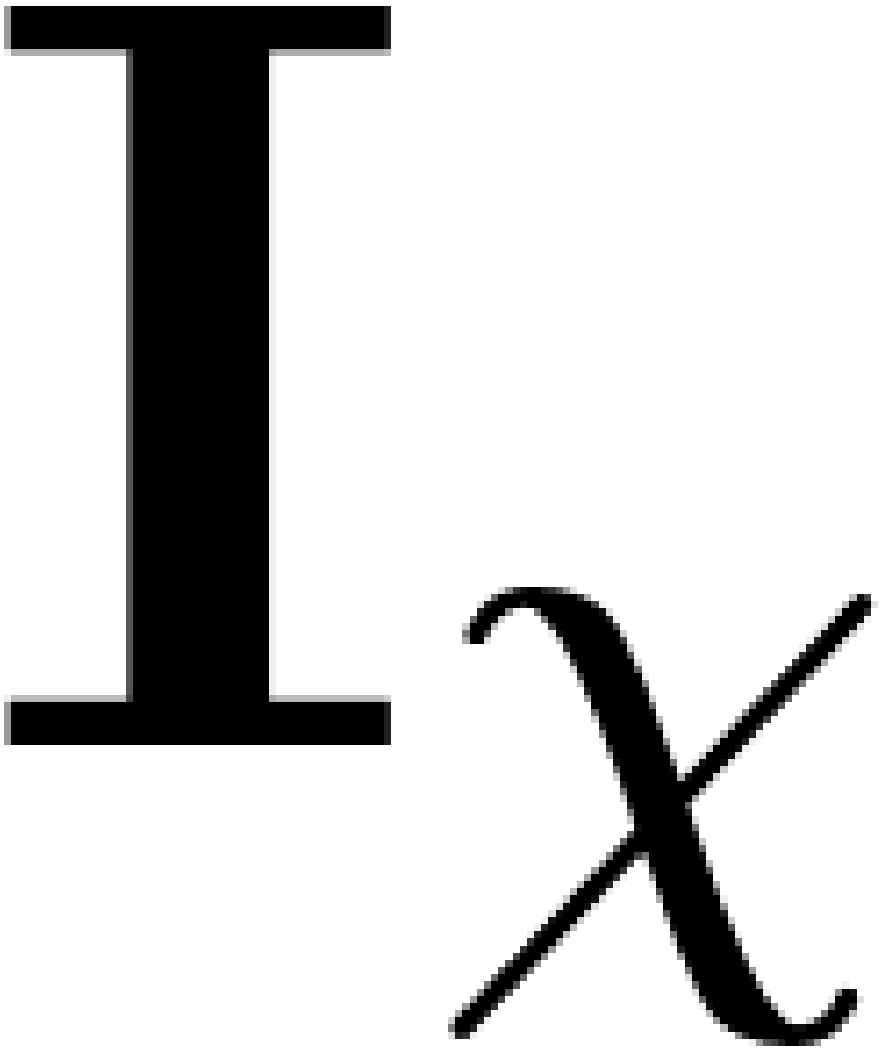

where 3.5 km/sec is a typical Rayleigh wave group velocity. All arrival times: ,

and correspond to the triggered on-condition (binary one) using the characteristic functions

for the P , SV , and SW phases respectively. For the definition of the other threshold functions, , and details of how the appropriate (de-) trigger thresholds are set, see the supplementary tables 1 and 2. For a benchmark of the algorithm, kindly refer to the supporting information text.

Example Earthquakes

First, we demonstrate the effectiveness of our single-station approach by testing on a set of known earthquakes selected from the U.S. Geological Survey (USGS) earthquake catalog. We use three-component seismograms recorded at a quiet station in Albuquerque, New Mexico, USA (**IU-ANMO**). We identify six different events (M_w >6) with station-earthquake azimuth and epicentral distance ranging from 30° to 120° (see s**upplementary figure 1 and supplementary table 1**). For each event, polarization analysis is applied to an hour-long record: a time duration long enough to observe first arriving body-waves and fundamental mode surface waves. A time- series of polarization traces, computed from the three-component seismogram, is then interpreted, enabling phase detection and allowing estimation of wave propagation direction. We notice that robust phase-detection requires the original waveform data to be filtered using a high-pass frequency of

0.1 Hz and a band-pass frequency of 0.006-0.2 Hz to improve the detection of body waves and surface waves, respectively. When comparing observed phase-arrival time using our detector with the predicted arrival time, we compute the predicted arrival time with a 1-D earth model using event parameters obtained from the USGS catalog (e.g., earthquake location, origin time, and magnitude). All seismograms are normalized by the maximum amplitude in the hour-long record for display purposes only (the vector sum is used for normalizing horizontal channels).

Limits of Seismic Detector

We test our single-station detector using a few events recorded at station ANMO (see Table 1). For the M7.6 event located in Nikolskoye, Russia, we are able to correctly identify the major seismic phases: P, S and Surface Waves (**supplementary figure 2**). Likewise, our estimate of the event to station azimuth is also correctly calculated from the largest principal axes. Along with the epicentral distance evaluated using the relative phase delay between the body wave phases (S-P time), we correctly locate the epicenter of the test events (**supplementary figure 3**). For teleseismic events to be correctly located by the single seismometer, the magnitude of all candidate events must be larger than Mw 6.0.

$$\triangle < 90$$

In our test-cases, the azimuth and epicentral distance for shallow teleseismic events (<50km) at moderate distances () is well constrained (**supplementary figure 3a and 3b**). However, when the events are deeper or farther away, the misidentification of the first arriving phase, weak excitation of the surface wave, or propagation complexities due to anisotropy (Laske & Masters, 2000) can lead to an estimation bias in the source location caused by an incorrect estimate of azimuth or epicentral distance (**supplementary figure 3c and 3d**). One approach to minimizing the error would involve incorporating information from multiple phases or the joint application of the coherence technique (Agius & Galea, 2011; Roberts et al., 1989). While the accuracy of our results depends on source-depth and propagation complexity, overall, the algorithm shows good performance for most of the candidate events. For brevity, we show detailed results for selected events only. A complete analysis of all test cases, including 2018 earthquakes recorded on the western African network is shown **supplementary figure 4, 5 & 6**).

Supplementary Table 1: Earthquake parameters (7 exemplary events) used to test the algorithm at station IU-ANMO and testing results.

Event No.	Mag.	Time (UTC)	Location	Coordinates (Lat, Lon)
1	**7.3**	**2018-12-20**	**Nikol'skoye, Russia**	**55.099, -106.457**
2	**7.2**	**2004-09-05**	**Shingu, Japan**	**33.070, 136.735**
3	**7.3**	**2019-07-14**	**Laiwui, Indonesia**	**-0.586, 128.034**
4	7.9	2018-09-06	Suva, Fiji	-18.474, 179.350
5	7.5	2018-01-14	Acari, Peru	-15.768, -74.709
6	**7.1**	**2018-11-30**	**Anchorage, Alaska**	**61.346, -149.955**
7	6.5	2016-10-30	Norcia Italy	42.862, 13.096

	Distance	Distance	Azimuth	Azimuth	Error	Error	Error	Error
Event	$\boldsymbol{\Delta^{\alpha}}$	$\boldsymbol{\Delta^{0,1}}$	$\boldsymbol{\Phi^{\alpha}}$	$\boldsymbol{\Phi^{0}}$ **(μοδε)**	**Distance** $\boldsymbol{\varepsilon\Delta^{0}}$	**Distance** $\boldsymbol{\varepsilon\Delta^{0}}$	**Distance** $\boldsymbol{\varepsilon\Delta^{1}}$	**Azimuth** $\boldsymbol{\varepsilon\ \Phi^{0}}$ **(μοδε)**
1	**62°**	61°	**69°**	68° (68°)	1%	1%	46%	2% (1%)
2	**90°**	95°	**47°**	62° (64°)	5%	5%	50%	32% (36%)
3	**119°**	88°	**50°**	37° (44°)	64%	64%	26%	24% (11%)
6	**38°**	48°	**114°**	63° (76°)	25%	25%	62%	44% (33%)

Δ^{a} : Actual distance in degrees between event and station.

$\Delta^{0,1}$: Observed distance in degrees between station and event using S-P time (0) or SW-S time (1).

$\epsilon^{0,1} = \frac{|^{0,1} - {}^{a}|}{{}^{a}}$: The normalized error between observed distance and true distance between station and event using S-P time (0) and SW-S (1) time respectively.

Φ^{a}: Actual angle from events to the station.

Φ^{0}: Observed azimuth from events to station from the distribution of azimuth using mean (node).

Supplementary Table 2: (De-) Trigger thresholds used to translate polarization attributes to binary characteristic functions for phase detection (e.g. Russia M 7.3).

Function	Description	Trigger (>Percentile)	Detrigger (<Percentile)
	Strength of Linearity	80%	75%
		e.g. 0.63	0.56
	P Energy	70%	65%
		0.62	0.55
	S Energy	65%	60%
		0.83	0.76
	P Angle (<)	20%	25%
		46.86	55.61
	S Angle (<)	10%	15%
		58.43	65.65
	Surface wave (<)	80%	85%

Supplementary Table 3. Attributes used for Phase Detection

Method	Attribute	Description	Equation
Energy Analysis		Total energy	
		Vertical energy	
		Horizontal energy	
Polarization Analysis		Eigenvector of the dominant particle motion	
	,	Strength of linear and elliptical polarization	
		Linearity of polarization	
		Azimuth	
		Incidence angle	

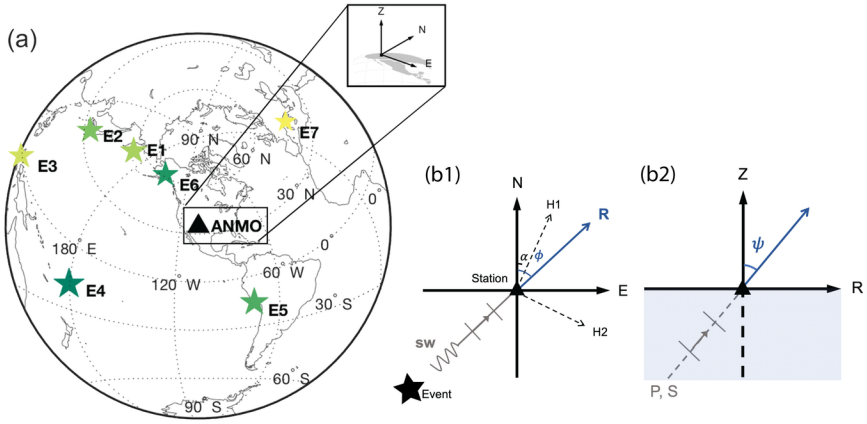

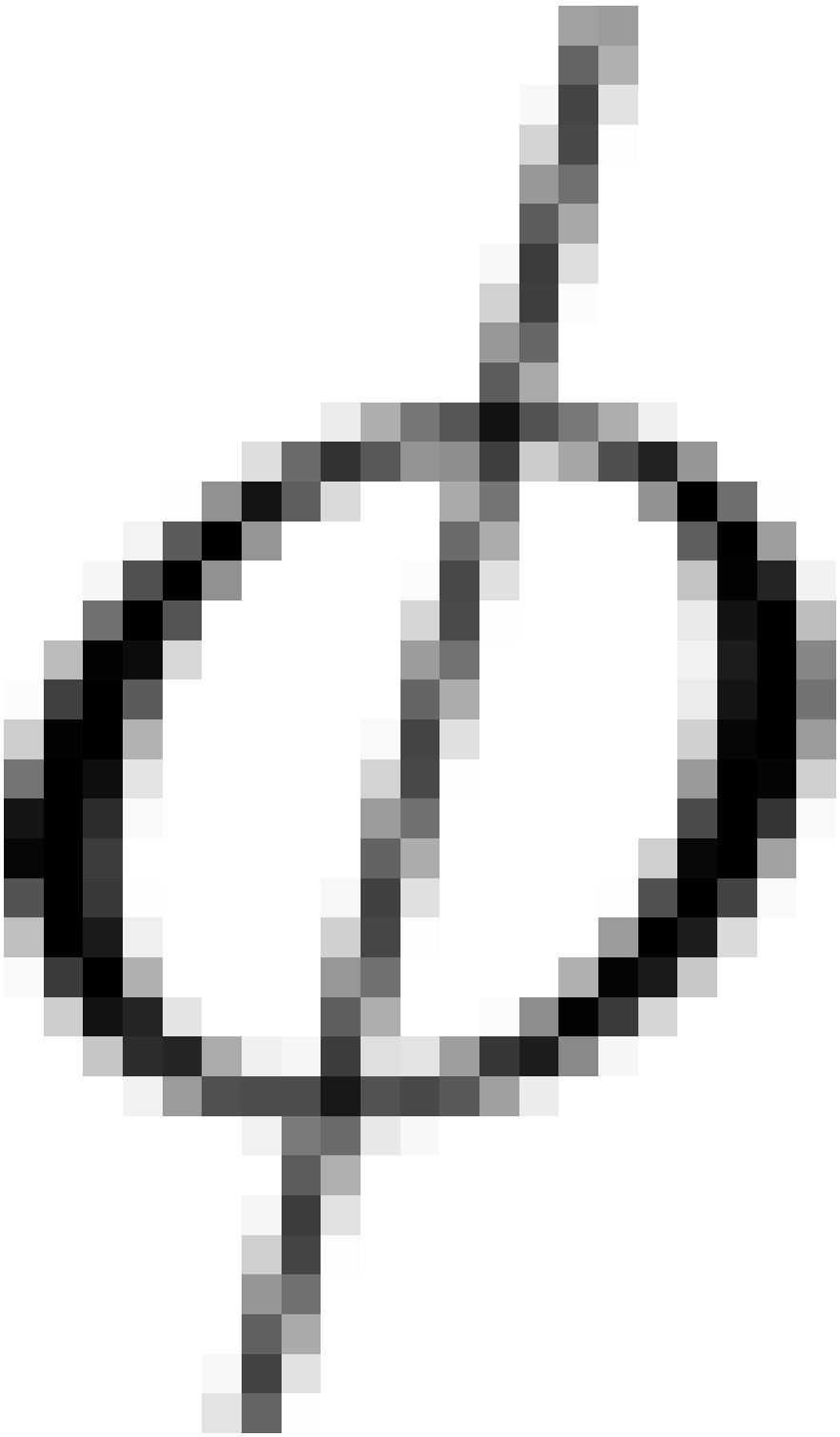

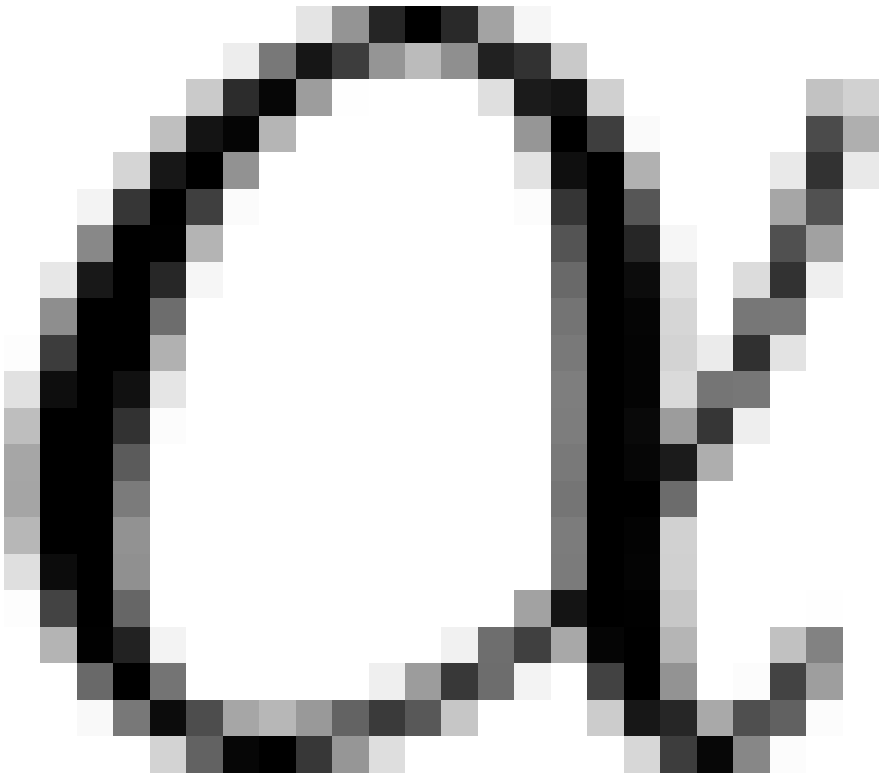

$\alpha = 0°, 90°$

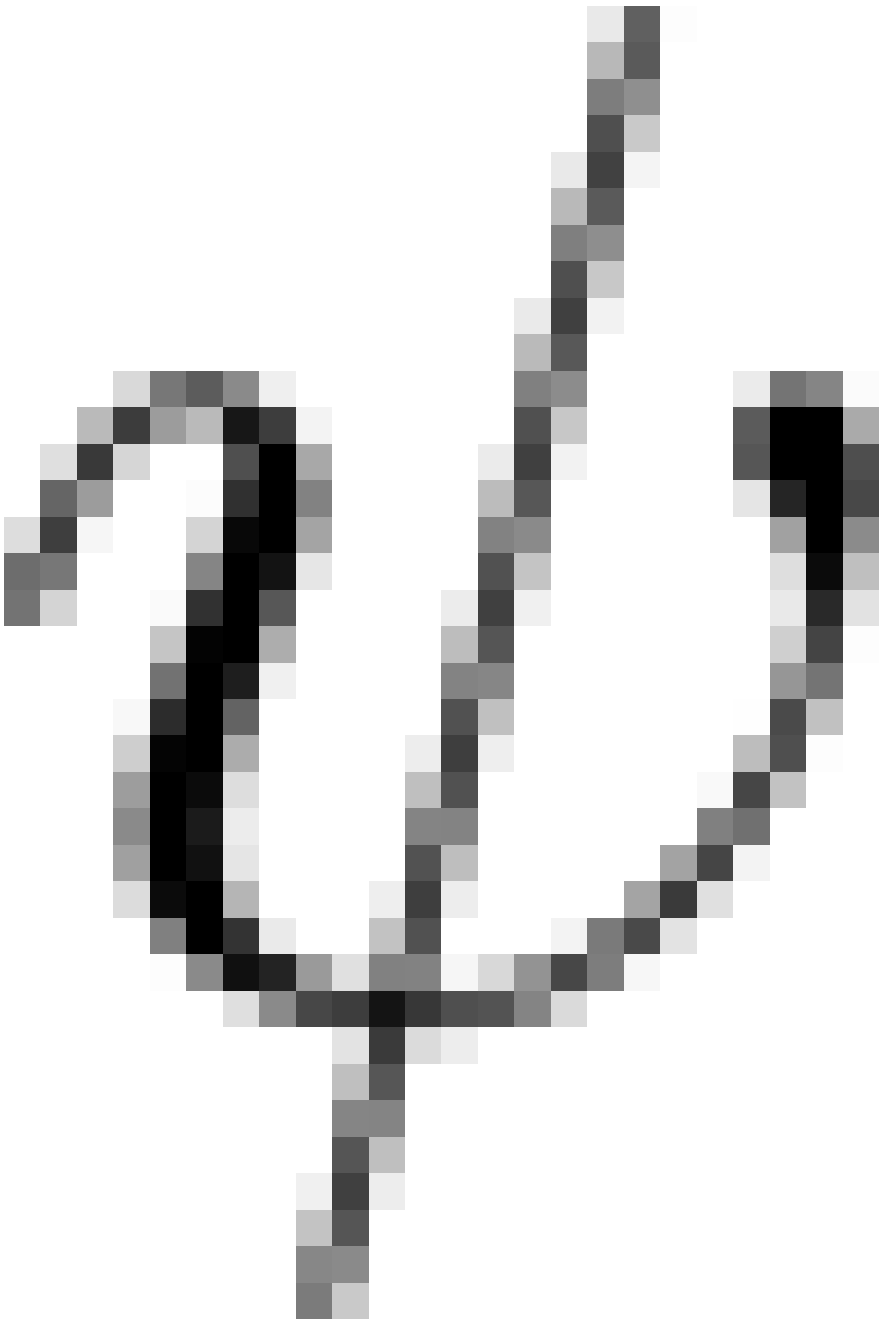

$$\psi = 0^{\circ}$$

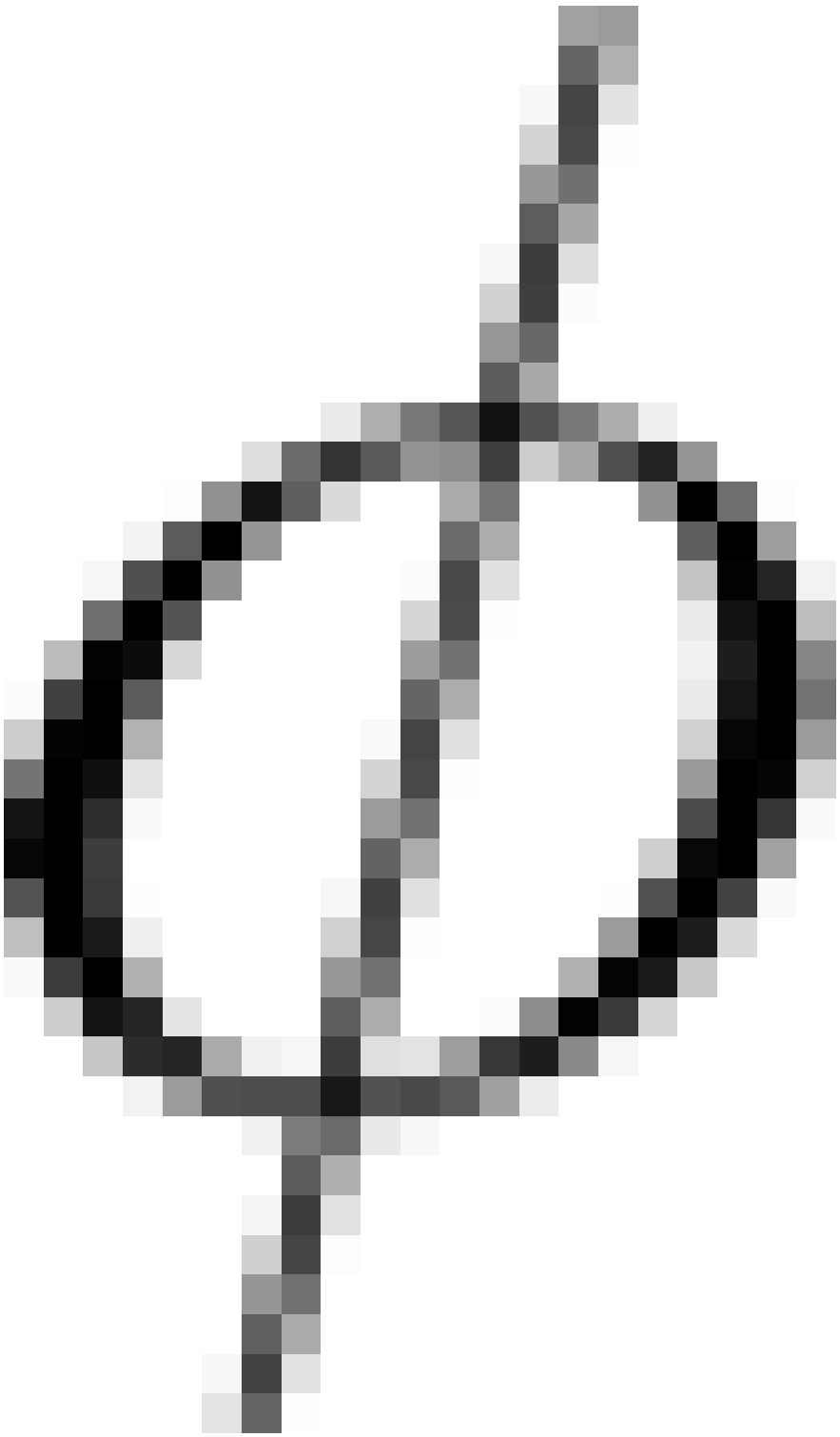

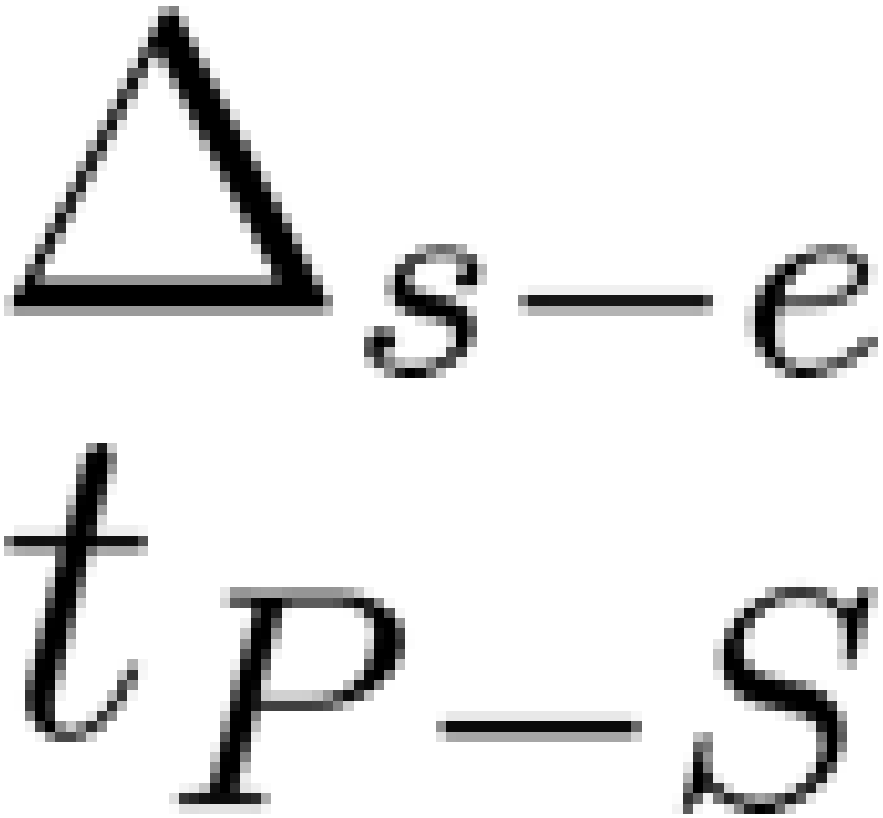

Supplementary Figure 1. Orientation of seismic channels at station ANMO (triangle) in cartesian coordinates and the exemplary earthquake (stars) used to demonstrate the single-station locator, showing the horizontal (b1) and vertical planes (b2) of wave polarization for surface waves (SW) and body waves (BW: P and S) respectively. (b1) The Azimuth

of the source-earthquake great circle path in plain view, measured relative to the two horizontal channels (H1 & H2) of the seismic station, with the H1 channel oriented at an angle, , measured clockwise from north, and H2 perpendicular to H1. In our reference frame, coordinates N and E are oriented at respectively. (b2) Incidence angle,, in elevation view, measured clockwise from vertical (here a P or S wave arriving perfectly vertical from below the station would have . In single-station source location, arrival direction can be determined by using P (BW) or Rayleigh (SW) to determine and the station-earthquake distance is determined by the P-S delay time , following the successful phase identification (see supplementary figure 3 for E1).

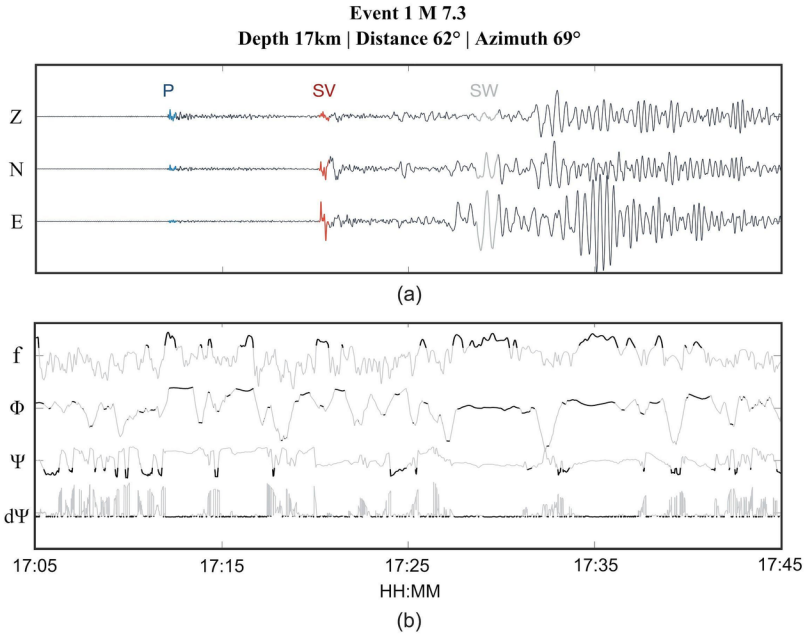

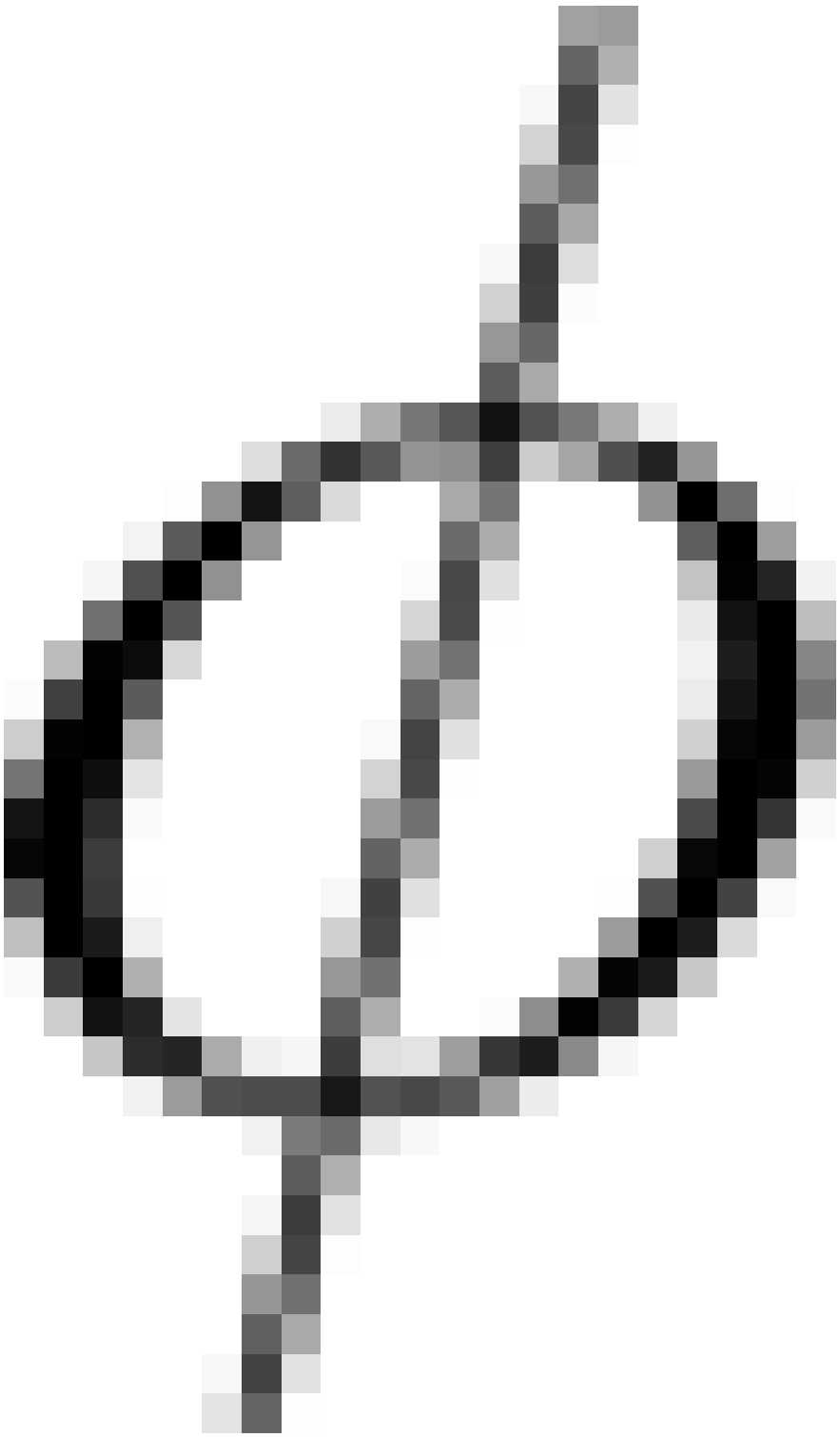

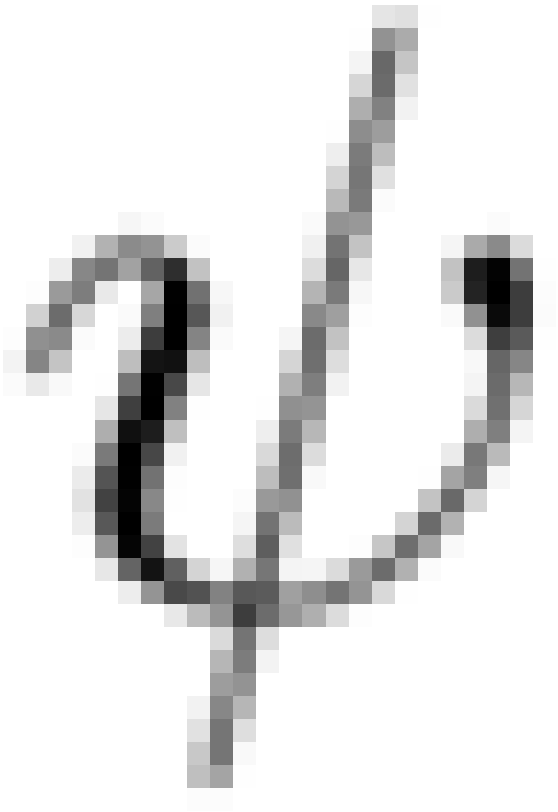

Supplementary Figure 2. (a) Three-component seismogram recorded at station ANMO, showing the unfiltered teleseismic P-wave arrival from a magnitude 7.3 earthquake with origin time Dec 20, 2018, in Nikolskoye, Russia with (E1 on Figure 1). The dashed line indicates the exact arrival time of the first arriving P (blue) and S (red) waves. (b) Application of polarization analysis on the filtered signal (BW using high-pass and SW using a bandpass). Each trace (light grey) represents an attribute used for phase detection with all triggered periods marked in black. Specifically, f and

represent the linearity of polarization and azimuth, with

and

representing the incidence angle and the stability of the calculated angle.

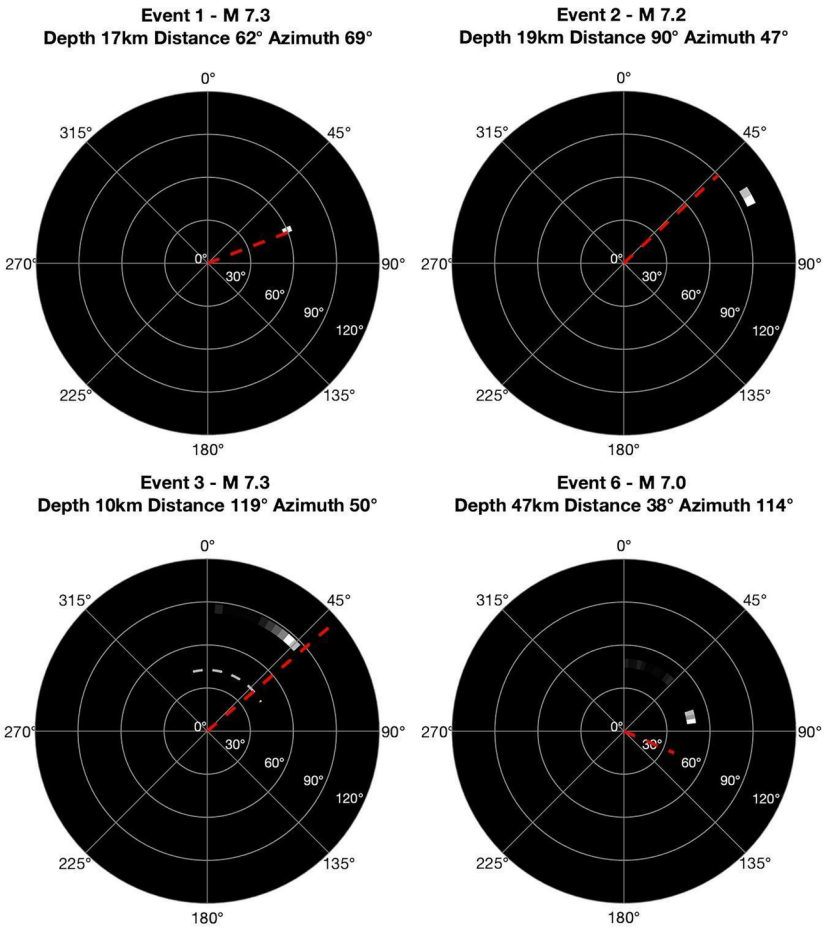

Supplementary Figure 3: Successful application of the multi-attribute polarization technique to the source location of four earthquakes (see Figure 3). The actual (red) and estimated distribution (polar histogram) of azimuth and epicentral distance demonstrate that a single-station event location is possible. For events within 100°, the epicentral distance is computed using the relative P-S delay time comparing the relative P-S delay time with the 1-D Earth model of (Snoke, 2009) using the*taup* software tool (Crotwell et al., 1999). For teleseismic events with an epicentral distance greater than 100° (Event 3), the relative S-SW delay time is used instead (the initial result using P-S delay time marked with a grey dashed line). See Fig. S1 for the result of anomalous events listed in Table 1.

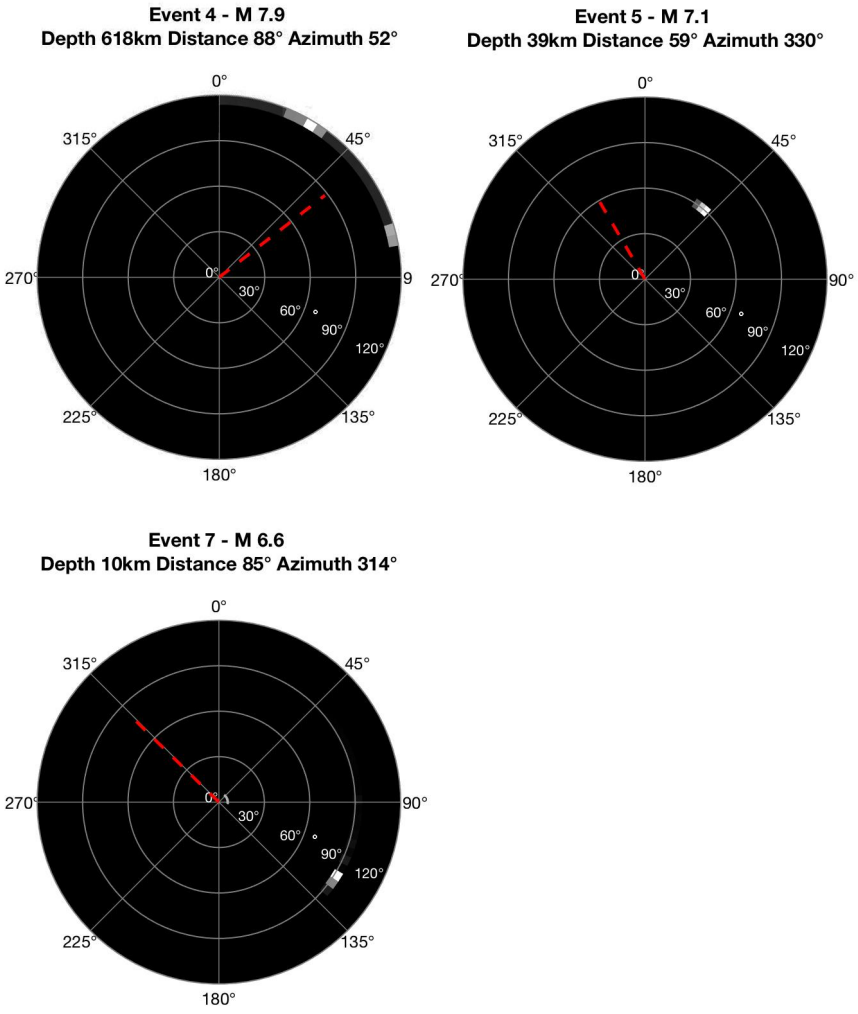

Supplementary Figure 4a. Single-station location using polarization attributes. Events with large bias showing types of errors for 3 test cases (similar to Figure 4).

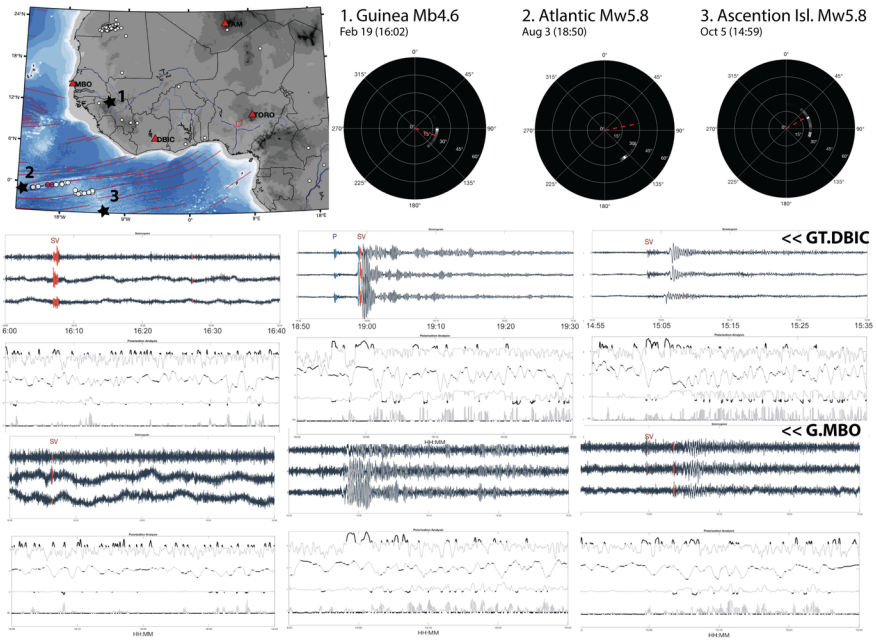

Supplementary Figure 4b. Demonstration of single-station location for three earthquakes in 2018 using stations: GT.DBIC and G.MBO (inset map). (Left -1) Guinea event (Middle-2) Central Mid Atlantic, and (Right-3) Ascension Island event. Location and phase identification for events 2 and 3 are better than for event 1. Only a single phase is identified for the Guinea event (compare with Fig. 4 for details).

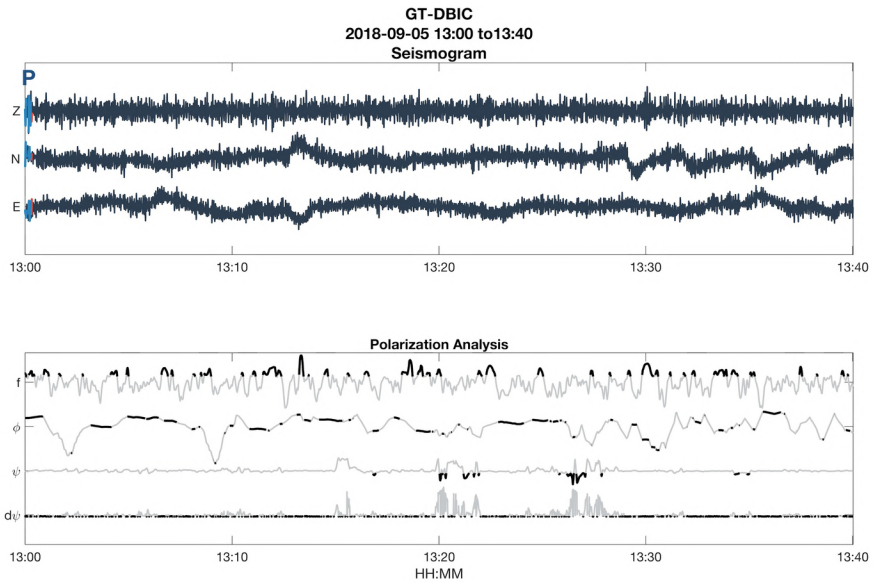

Supplementary Figure 5a. Scan anecdotal event 1: Sept 5. 13:30 UTC.

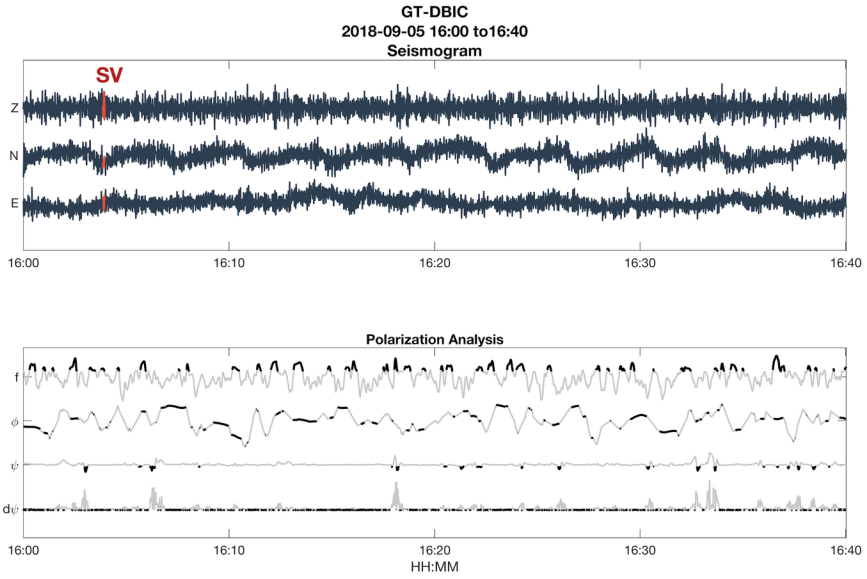

Supplementary Figure 5b. Scan anecdotal event 2: Sept 5. 16:30 UTC.

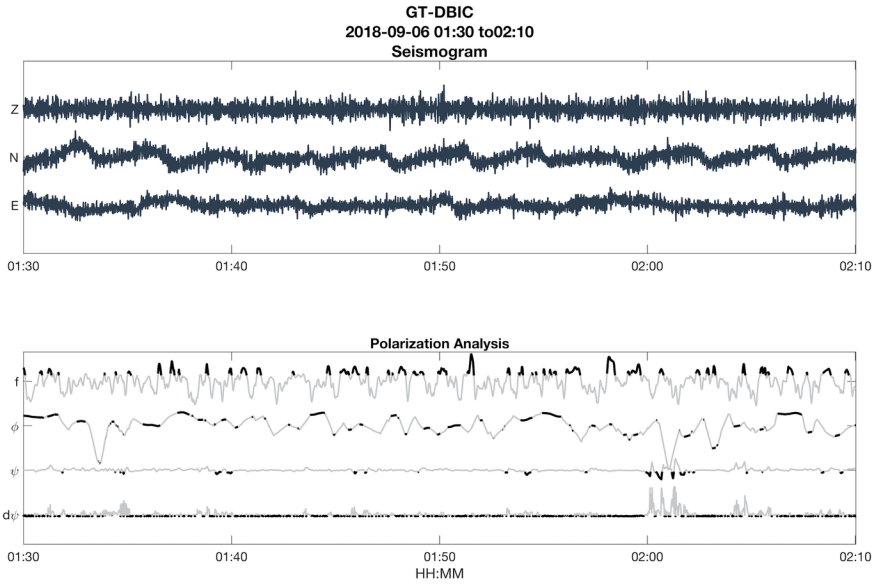

Supplementary Figure 5c. Scan anecdotal event 3. Sept 6. 01:30 UTC

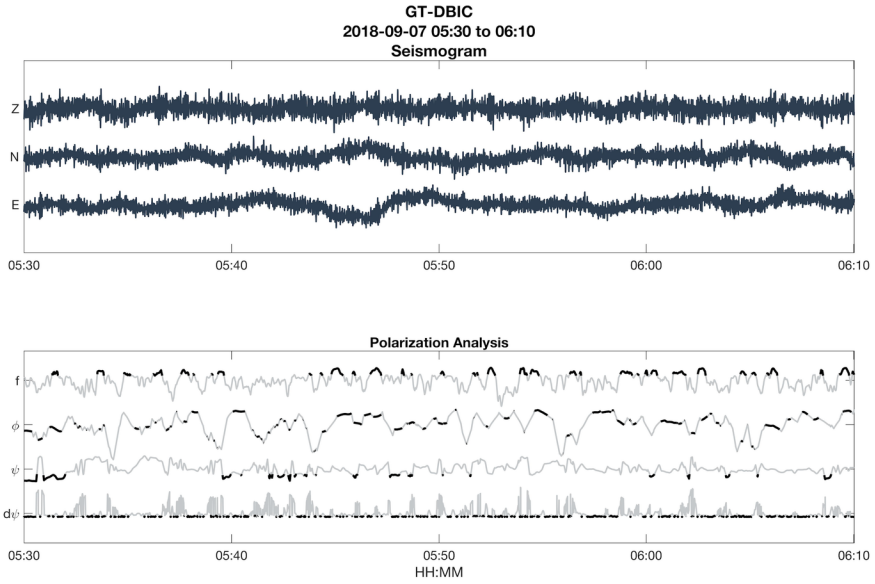

Supplementary Figure 5d. Scan anecdotal event 4. Sept 7. 05:30 UTC

References

Agius, M. R., & Galea, P. (2011). A Single-Station Automated Earthquake Location System at Wied Dalam Station, Malta. *Seismological Research Letters*,*82*(4), 545–559. https://doi.org/10.1785/gssrl.82.4.545

Crotwell, H. P., Owens, T. J., & Ritsema, J. (1999). The TauP Toolkit: Flexible seismic travel-time and ray-path utilities. *Seismological Research Letters*, *70*(c), 154–160. Retrieved from http://www.seis.sc.edu/downloads/TauP/taup.pdf

Ekström, G. (2006). Global detection and location of seismic sources by using surface waves.*Bulletin of the Seismological Society of America*, *96*(4), 1201–1212. https://doi.org/10.1785/0120050175

Gou, T., Huang, Z., Zhao, D., & Wang, L. (2019). Structural Heterogeneity and Anisotropy in the Source Zone of the 2018 Eastern Iburi Earthquake in Hokkaido, Japan.*Journal of Geophysical Research, [Solid Earth]*,*124*(7), 7052–7066. https://doi.org/10.1029/2019JB017388

Havskov, J., & Ottemöller, L. (2010). Location. *Routine Data Processing in Earthquake Seismology*. https://doi.org/10.1007/978-90-481-8697-6_5

Kennett, B. L. N., Engdahl, E. R., & Buland, R. (1995). Constraints on seismic velocities in the Earth from traveltimes. *Geophysical Journal International*,*122*(1), 108–124. https://doi.org/10.1111/j.1365-246X.1995.tb03540.x

Kogan, M. G. (2003). The 2000 M w 6.8 Uglegorsk earthquake and regional plate boundary deformation of Sakhalin from geodetic data. *Geophysical Research Letters*,*30*(3), 227. https://doi.org/10.1029/2002GL016399

Laske, G., & Masters, G. (2000). Surface-wave polarization data and global anisotropic structure, (1998), 508–520.

Roberts, R. G., Christoffersson, A., & Cassidy, F. (1989). Real-time event detection, phase identification and source location estimation using single station three-component seismic data. *Geophysical Journal International*,*97*(3), 471–480. https://doi.org/10.1111/j.1365-246X.1989.tb00517.x

Snoke, J. a. (2009). Traveltime Tables for iasp91 and ak135. *Seismological Research Letters*, *80*(2), 260–262. https://doi.org/10.1785/gssrl.80.2.260

Wang, F., Fan, X., Yunus, A. P., Subramanian, S. S., & Huang, R. (2019). Coseismic landslides triggered by the 2018 Hokkaido, Japan (Mw 6.6), earthquake: spatial distribution, controlling factors, and possible failure mechanism.*Landslides*, (1). https://doi.org/10.1007/s10346-019-01187-7

Zhang, S., Li, R., Wang, F., & Iio, A. (2019). Characteristics of landslides triggered by the 2018 Hokkaido Eastern Iburi earthquake, Northern Japan. *Landslides*,*16*(9), 1691–1708. https://doi.org/10.1007/s10346-019-01207-6

frontiers

On the Origin of Orphan Tremors & Intraplate Seismicity in Western Africa

Tolulope M. Olugboji[1*], Manoochehr Shirzaei[2], Yingping Lu[1], Adekunle Adepelumi[3], Folarin Kolawole[4, 5]

[1]University of Rochester, United States, [2]Virginia Tech, United States, [3]Obafemi Awolowo University, Nigeria, [4]University of Oklahoma, United States, [5]BP (United States), United States

Submitted to Journal:
Frontiers in Earth Science

Specialty Section:
Solid Earth Geophysics

Article type:
Hypothesis and Theory Article

Manuscript ID:
716630

Received on:
28 May 2021

Journal website link:
www.frontiersin.org

Conflict of interest statement

The authors declare that the research was conducted in the absence of any commercial or financial relationships that could be construed as a potential conflict of interest

Author contribution statement

TBD

Keywords

tremors, InSAR (Interferometric Synthetic Aperture Radar), Aeromagnetic data, seismology, polarization

Abstract

Word count: 164

On September 5-7, 2018, a series of tremors were reported in Nigeria's capital city, Abuja. These events followed a growing list of tremors felt in the stable intra-plate region, where earthquakes are not expected. Here, we review available seismological, geological, and geodetic data that may shed light on the origin of these tremors. First, we investigate the seismic records for parent location of the orphan tremors using a technique suitable when a single-seismic station is available such as the Western Africa region, which has a sparse seismic network. We find no evidence of the reported tremors within the seismic record of Western Africa. Next, we consider the possibility of a local amplification of earthquakes from regional tectonics, reactivation of local basement fractures by far-field tectonic stresses, landward continuation of oceanic fracture zones, or induced earthquakes triggered by groundwater extraction. Our assessments pose important implications for understanding Western Africa's intraplate seismicity and its potential connection to tectonic inheritance, active regional tectonics, and anthropogenic stress perturbation.

Contribution to the field

In our manuscript, we investigate the origin and cause of the Sept 5-7, 2018 intense shaking reported in Abuja, the capital city of Nigeria, West Africa, a region not known to generate moderate or large earthquakes. We review seismicity (most from ~ 40 years ago), tectonics, local geology, and surface deformation in the region. We evaluate the local basement structure in Abuja demonstrating how structures inherited from past tectonics may be critically oriented for reactivation within the present-day stress field and the presence of a sedimentary cover that is significant enough to amplify seismogenic shaking

Ethics statements

Studies involving animal subjects

Generated Statement: No animal studies are presented in this manuscript.

Studies involving human subjects

Generated Statement: No human studies are presented in this manuscript.

Inclusion of identifiable human data

Generated Statement: No potentially identifiable human images or data is presented in this study.

Data availability statement

Generated Statement: Publicly available datasets were analyzed in this study. This data can be found here: https://doi.org/10.17632/W7KKG3G37D.1.

On the Origin of Orphan Tremors & Intraplate Seismicity in Western Africa

Olugboji, T.[1,*], Manoochehr Shirzaei[2], Yingping Lu.[1,3*], Adepelumi, A.A.[4], Kolawole, F.[5,6]

[1]*Department of Earth and Environmental Sciences, University of Rochester, NY*

[2]*Department of Geosciences, Virginia Tech*

[3]*Goergen Institute for Data Science, University of Rochester, NY*

[4]*Department of Geology, OAU, Ife, Nigeria*

[5]*School of Geology and Geophysics, University of Oklahoma, Oklahoma*

[6]*Now at BP America, Houston, Texas*

[*] *Corresponding author: tolugboj@ur.rochester.edu*

Abstract

On September 5-7, 2018, a series of tremors were reported in Nigeria's capital city, Abuja. These events followed a growing list of tremors felt in the stable intra-plate region, where earthquakes are not expected. Here, we review available seismological, geological, and geodetic data that may shed light on the origin of these tremors. First, we investigate the seismic records for parent location of the orphan tremors using a technique suitable when a single-seismic station is available such as the Western Africa region, which has a sparse seismic network. We find no evidence of the reported tremors within the seismic record of Western Africa. Next, we consider the possibility of a local amplification of earthquakes from regional tectonics, reactivation of local basement fractures by far-field tectonic stresses, post-rift crustal relaxation, landward continuation of oceanic fracture zones, or induced earthquakes triggered by groundwater extraction. Our assessments pose important implications for understanding Western Africa's intraplate seismicity and its potential connection to tectonic inheritance, active regional tectonics, and anthropogenic stress perturbation.

Introduction

On September 5-7, 2018, a series of low-magnitude tremors hit Nigeria's capital city in Mpape, Abuja ("Government Report," 2018). These events followed a series of earthquakes felt in the region since 1933, a stable, intraplate setting, otherwise not being earthquake-prone (Ofonime U. Akpan et al., 2014; Ofonime Umo Akpan & Yakubu, 2010; Tsalha et al., 2015). This seismicity puts in the spotlight the issue of seismic hazards in the Western Africa region and the need for an improved seismic monitoring network (K. U. Afegbua et al., 2019; Alaneme & Okotete, 2018). Nigeria is located in the southern part of the Neoproterozoic Trans-Saharan Mobile Belt, separating the Archean West African Craton, Congo Craton, and the Archean-Proterozoic Sahara Metacraton. Within this mobile belt, a large continent-scale system of elongate rift basins (aulacogens) developed during the Cretaceous, among which is located the Benue Trough on whose flank the Abuja city is located (Figure 1a). The extent of areas that historical seismicity felt in Nigeria encompasses regions within the failed rifts and areas of the exposed basement on the flanks of the rift basins (figure 1a).

Compared to historical events, the series of shakings reported on Sept, 2018 is located within the Northern edge of Abuja. Because the capital city of Abuja is highly populated and relatively affluent, most of the citizens felt considerable shaking and this was reported by the local news agencies and picked up by increased social media activity. Although the local population felt these events, very little observational evidence exists for the origin of the shaking and its connection to local geology, or regional tectonics. Here, we present the available geological and geophysical constraints that may offer clues about the shaking and examine the available seismic, geologic, and geodetic measurements and discuss several viable hypotheses regarding the origin of the felt shaking, connected to the local or regional tectonics and anthropogenic activities. In particular, we evaluate the hypotheses that these events are due to 1) local amplification of earthquakes from regional tectonics, 2) distant teleseismic events large enough to be felt in western Africa, 3) reactivation of local basement fractures by far-field tectonic stresses, post-rift crustal relaxation, or landward continuation of oceanic fracture zones, or 4) local anthropogenic activities such as groundwater extraction.

A comprehensive search of the global earthquake catalog in the decade leading up to Sept, 2018, does not turn up any events located within Nigeria. In and around the Western African region, most of the events are clustered around oceanic transform faults, with only a few inland earthquakes. Similarly, all earthquakes in 2018 occurred along the oceanic transform fault, except for a single event on Feb. 19, located in the country of Guinea about 10 degrees northwest of Nigeria (Figure 1). Therefore, we examine the available seismic data from the Nigerian seismic network (K. U. Afegbua et al., 2011), supplementing them with seismic stations from the western African region where long-term real-time monitoring is available. We conduct a rigorous search of the seismic record using a single-station detector method to

examine the first two hypotheses, which investigate the possibility of the shaking being related to distant earthquakes and their ability to reactivate pre-existing fault systems that may be preferentially primed for failure (Han et al., 2017; Neves et al., 2018). We then complement the seismic investigation with other geological and geophysical datasets. Surface geology and basement structure is investigated using high resolution satellite images and aeromagnetic data, and the observed patterns compared to the inferred prevailing stress field as well as the general trends dictated by the opening and closure of the failed rifts located close to the Abuja capital city. A final analysis explores the anthropogenic controls on earthquake nucleation and whether these may be related to the hydrological cycle within Nigeria. We measure surface deformation using Interferometric Synthetic Aperture Radar (InSAR) and correlate the observed patterns with the ongoing anthropogenic activities such as groundwater pumping and the addition of dams in the study area. Overall, the assessments presented in this study pose important implications for understanding western Africa's intraplate seismicity and its connection to regional tectonics and local geology.

Method

Single-Station Seismology

Ideally, the detection of a low-magnitude local or regional event would require a proximal high-quality seismic array. Western Africa, on the other hand, has a sparse distribution of real-time seismic stations. Even recently deployed small-aperture seismic arrays located in Western Africa, e.g., Nigeria (Kadiri Umar Afegbua et al., 2011) and Ghana (Ahulu & Danuor, 2015) do not currently archive data on global waveform databases and only a few are real-time. Therefore, we use a single-station location method that is based on polarization analysis using eigen-decomposition of ground displacement (Bai & Kennett, 2000; J. Park et al., 1987; Simons et al., 2009; Vidale, 1986) for event detection, seismic phase identification (Earle, 1999), and source localization (Böse et al., 2017). Alternative methods such as beamforming analysis, which is widely applied to pin-pointing earthquake source direction (Nakata et al., 2019; Rost, 2002; Rost et al., 2006) is challenging to apply because of the sparsity of high-quality, continuously recording, small-aperture seismic arrays present at regional distances to the location of the largest reported shaking.

The single-station location technique is based on the same principle for which polarization analysis is most commonly used, i.e., orienting seismometers on the bottom of the sea-floor (Doran & Laske, 2017; Scholz et al., 2017; Stachnik et al., 2012; Zha et al., 2013) or identifying misoriented horizontal channels (Ojo et al., 2019). Used in this mode, the arrival direction (azimuth) and the distance of a seismic event can be inferred from a three-channel seismogram recorded on a single-station on the African continent. The geographical orientation of the seismic channels is then determined given a known arrival direction of a particular seismic phase (often the compression and Rayleigh waves). In the

earthquake-location mode, however, the idea is reversed. We assume the channel orientations are known (or can be corrected for), then, in principle, we fix the source orientation by determining the azimuth of the incoming waves. The key idea is to identify the polarization of particular seismic phases which are parallel to the wave propagation (e.g. compressional and Rayleigh wave phases) and use this to determine the wave-arrival azimuth. A differential time between the first arriving compressional wave and other phases (e.g. S, Love, and Rayleigh), in conjunction with a given earth model, prescribes the epicentral distance and completes the process - providing coordinates of the earthquake.

The adaptation of polarization analysis for single-station event location (Agius & Galea, 2011; Böse et al., 2017; Frohlich & Pulliam, 1999; Magotra et al., 1987, 1989) increases the likelihood of detecting earthquakes with smaller magnitudes. In our adaptation, we incorporate benefits from the coherence (Vidale, 1986) and covariance technique (Jurkevics, 1988; S. Park & Ishii, 2018; Schulte-Pelkum et al., 2004), and include multimode identification (Bai & Kennett, 2000, 2001). Our idea bears some similarity to the technique proposed for locating Mars-quakes (Böse et al., 2017), or the identification of the source location of ambient seismic noise or micro-tremors (Koper & Hawley, 2010; Zha et al., 2013). We describe a successful application for locating the epicenter of moderate-to-large teleseismic earthquakes. We then describe the application to a few high-quality stations recording during the three days with the largest shaking i.e stations on the Geoscope network (Roult et al., 2010), the global seismic network (GSN) (Lay et al., 2002), and the Nigerian Seismic Network .

While single-station event location is sufficient for distinguishing between a teleseismic and a local/regional event, when more than one station is available, the uncertainty or bias (error) from a single-station detection can be improved by performing a second-stage association analysis (Ekström, 2006; Ringdal & Husebye, 1982; Shearer, 1994). This allows us to improve the confidence estimate for the location by comparing the estimated source locations from multiple stations when they are available. Suppose all the single-station locations agree (within uncertainty) that the hypothesized source location (Abuja, Nigeria) is not the epicenter of the detection, in that case, we can rule out this null hypothesis and explore the alternative hypothesis that the shaking is from a different source location (i.e. of teleseismic origin). We require only two stations to confirm detection for a particular source location. Application to the 360 polarization records derived from each of the five closest stations to Nigeria results in a space-time probability of a possible event detection (Böse et al., 2017) (see Appendix for a detailed discussion of technique).

Aeromagnetic Data Analysis

The largest shaking may have resulted from seismogenic slip on local faults or due to local amplification. To explore how local geology in and around Abuja may have contributed to significant shaking intensity, following standard practice, we analyze the subsurface structure

and the spatial distribution of the sedimentary cover. The Abuja area is located in low magnetic latitude. Thus, we first perform a reduction of the magnetic data to the magnetic equator (RTE, e.g., (Li & Oldenburg, 2001) using an IGRF 2005 model. This transformation corrects for the skewness of the magnetic anomalies due to the oblique angles of magnetization at large distances from the magnetic pole.

Afterward, we upward-continue the RTE-corrected aeromagnetic grid to remove noise and apply a vertical derivative filter to better resolve the gradients that correspond to the geological structure. Further, we estimate the distribution of depths to the top of the magnetic sources (i.e. crystalline basement) using the Source Parameter Imaging (SPI) method (Smith et al., 2002; Smith & Salem, 2005). Although this technique has an accuracy of ±20%, it can reliably show the relative spatial pattern of the depth of the burial of the magnetized basement (e.g., Kolawole *et al.*, 2018). We manually interpret the geological structure-related lineaments and plot rose diagrams to identify the dominant trends in both the satellite images and filtered aeromagnetic maps.

InSAR deformation field

To map the surface deformation, we use 80 SAR images acquired in the ascending orbit of the Sentinel-1A/B C-band satellites between 2018/01/19 and 2020/09/05. We performed an advanced multitemporal SAR interferometric analysis to retrieve rates and time series of surface deformation over the study area. The analysis began with co-registering SLC images to a reference image, which includes a standard matching algorithm using a Digital Elevation Model (DEM), precise orbital parameters, and amplitude images (Sansosti et al., 2006). For the Sentinel-1A/B datasets, the step above is followed by an enhanced spectral diversity (ESD) approach (M. Shirzaei & Bürgmann, 2017; Yagüe-Martínez et al., 2016). Using this dataset, we generate a set of high-quality interferograms, considering only those with short perpendicular and temporal baselines. We also apply a multi-looking operator of 32 and 6 pixels in range and azimuth to obtain a ground resolution cell of ~75 m × 75 m. To calculate and remove the effect of topographic phase and flat earth correction (Franceschetti & Lanari, 2018), we used a 1-arcsecond (~30 m) Shuttle Radar Topography Mission DEM (Farr et al., 2007) and precise satellite orbital information. To identify the elite (i.e., less noisy) pixels, we only consider pixels with an average temporal coherence larger than 0.65. To retrieve the absolute (unwrapped) phase values, we applied a Minimum Cost Flow (MCF) algorithm adapted for sparsely distributed elite pixels. Although the precise orbits are used, a few interferograms were still affected by a ramp-like signal, which were corrected by fitting a 2nd order polynomial to their unwrapped phase (Manoochehr Shirzaei & Walter, 2011). We further applied several wavelet-based filters to correct for effects of spatially uncorrelated topography error and topography correlated atmospheric delay (M. Shirzaei & Bürgmann, 2012). Subsequently, we applied a re-weighted least square approach iteratively to invert the corrected measurement of the unwrapped phase at each elite pixel and solve the time series of the surface deformation. We further reduce the effect of residual atmospheric errors by applying a high pass filter based on continuous wavelet transform to the time series of surface deformation at each elite pixel. Finally, we estimate the long-term line-of-sight (LOS) deformation rates as the best-fitting line slope to the time series of surface deformation at each elite pixel.

Data and Results

Earthquake Detection with a Sparse Network

We use the following station-selection criteria: (1) waveform data recorded during tremor activity archived and retrievable from a global waveform database, e.g., IRIS, (2) good back-azimuth coverage relative to Nigeria, (3) availability of three-channel seismograms necessary for polarization analysis, (4) high signal to noise ratio, (5) correct orientations for the horizontal channels or new analysis reflecting the proper orientations e.g., (Ojo et al., 2019). We select five stations that pass our selection criteria, and their locations provide relatively good azimuthal coverage around Nigeria (see Figure 1b and Table 1). We focus on the three days from September 5 - 7, 2018, when anecdotal reports agree on the strongest shaking in Nigeria, (1) three reports on Sept. 5: ~ 13:30, 16:30, and 19:00 UTC and (2) two on Sept. 6 and 7: 01:30, 05:30 UTC. We scan hour-long records of three-component seismograms at each station, allowing for a half-hour to extend detection duration. Our dataset results in 360 polarization records representing 72 hour-long records (for the 3 days) at each of the 5 stations. A preliminary data quality check based on a signal to noise detection of earthquakes in the global catalog reveals that only two of the stations in this region are particularly useful for seismic detection (i.e. G.TAM and G.DBIC). In particular, stations NJ.TORO, the closest station to the main interest area - Abuja - is very noisy and is impractical for detection on its own (see Figure 1a and 2). This analysis further highlights the challenge of earthquake location and the value of a single station event detector.

Null Detection & Other Coincidences: We analyze the continuous data stream in hour-long sections during the three days of the largest reported shaking. In this 3-day scan, we detect a notable event in the hour following 18:00 UTC on September 5th with good SNR on most stations (Figure 2). Our attempt to associate the other tremor sequences to either a previously undetected global or regional event proved inconclusive (supplementary figures 5a-d). For the Sept. 5 event, the stations detect P and S arrivals within only slight timing variations. We cross-reference our detection with the USGS earthquake catalog. The arrival time of the seismic phases is correctly matched with a source location that is consistent with the *M6.6 Hokkaido Eastern Iburi, Japanese* earthquake (Figure 3 and 4b). We note that this event is neither local nor regional (< 30 degrees) but clearly of teleseismic origin (compare Figure 4a,b with Figure 3). Despite the large station-earthquake distances (80 - 120 degrees), we detect clear body-wave and surface-wave phases on the high-quality stations located around Nigeria. Even for the station at the largest epicentral distance (GT-DBIC), strong PP and SS phases are visibly detected and identified by our phase detector (Figure 3).

The closest stations to the Japanese event are able to pick up at least one of the two direct P and S arrivals. For example, station II-RAYN demonstrates that our method provides effective picks for four of the incoming phases (*P, PP, S, SS, L, R: Figure 3*). At stations

MN-WDD and IU-FURI located at an epicentral distance less than 90°, we precisely identify all the main P and S arrivals except for the reflected *SS* phase. At station II-MBAR, which is even further away (>90°) from the source location, our method is still able to detect the diffracted phases (*Pdiff* and *Sdiff*). However, at station GT-DBIC which is located ~120° from Japan, we are unable to detect the first-arriving diffracted Pdiff waves and only able to detect the diffracted Sdiff phase (with a slight time shift compared to the travel time predictions using the ak135 Earth model) and the reflected PP and SS phase. Association of the single-station detections shows that three of the five stations (WDD, FURI, MBAR) provide a location match with an error $< 5^{\circ}$, while the other two stations (DBIC and RAYN) agree on the epicentral distance with some bias in the azimuth direction (Figure 5). This is clear evidence that the seismic event detected at all our stations is coincident in space and time with the teleseismic Japanese event reported by the global catalog and felt in Nigeria on September 5th.

Our search for a source-origin in West Africa was inconclusive, which may suggest a low magnitude event that may have been attenuated before being detected by the regional seismic network.We emphasize that of the five events reported in anecdotal records, we are able to associate a single event to a teleseismic earthquake originating in Hokkaido, Japan on Sept. 5, 2018 (18:07 UTC). This event, from far-away japan, triggered multiple landslides (~ 6,000) that lasted for a few minutes ((Kameda et al., 2019; Shao et al., 2019; F. Wang et al., 2019; Yamagishi & Yamazaki, 2018). None of the other tremors in the sequence identified by anecdotal records are conclusively associated with either a local or teleseismic event. We explore briefly, what explanation, if any, exists between the felt shaking and this landslide event. Alternatively, we evaluate how the local geology around Abuja could host the reactivation of existing faults. We also consider the possibility of induced earthquakes triggered by groundwater extraction.

Geological Framework from Aeromagnetic Data Analysis and Satellite Data

We integrate available surface and subsurface geological and geophysical datasets to constrain the first-order geological features in the Abuja area that could have localized or amplified ground shaking. First, we delineate satellite-scale fracture systems in basement outcrops using Google Earth satellite images at a spatial resolution of 5 m (e.g., (Kolawole et al., 2019). Then, we utilize high-resolution aeromagnetic data first to map sub-surface structural fabrics representing potential mega-scale fault lineaments in the granitic basement, then to model the distribution and thickness of the sedimentary over-burden (e.g., (Grauch & Hudson, 2007; Kolawole et al., 2018)). The aeromagnetic data used in this study was acquired country-wide between 2005 and 2007 by the Nigerian Geological Survey Agency (NGSA), with 500 m line spacing and 80 m mean terrain clearance. The aeromagnetic data was provided as a grid of 100 m cell size.

Delineated geological structures in the Abuja area

The satellite-scale fracture systems in the basement outcrops, mapped in the satellite images of the Abuja area (Figures 6a-b) show dominant trends of 049°±3.6° (NE-SW) and 136°±3.7°(NW-SE) (Figure 6c). Also, the subsurface basement lineaments, delineated in filtered aeromagnetic data (Figure 6d) show dominant trends of 048°±6.4° (NE-SW), 124°±6.1° (NW-SE), and 086°±5.4° (E-W) (Figure 6e). Further, our depth-to-basement map, generated from the SPI transform of the aeromagnetic data (Figure 6f-g) shows that most of the Abuja area and mainly the areas where the tremor was felt are located within a small sedimentary basin. The thickness of this sedimentary cover ranges between ~200 - 800 m (Figure 6g). Although the three prominent trends (NE, NW, and E-W) can be observed in the northern half of the area where basement outcrops dominate, the NE-trending lineaments appear to dominate the southern part where the basin is located (Figure 6d).

InSAR Ground Deformation Map

Figure 7 shows the rate of LOS displacement field and selected time series at the sites of rapid subsidence. The negative values (cool colors) correspond with movement away from satellite, hereafter, subsidence. The map is characterized by widespread subsidence up to 35 mm/yr. Roughly the zone of subsidence is bounded by the administrative divides, suggesting an anthropogenic drive. A rapidly declining trend characterizes the selected time series of LOS displacement at sites (b), (c) and (d) until 2020. The slightly rising time series (Fig. 7e) also follows a similar pattern, whose rising trend is interrupted by 2020. This behavior change might be attributed to the COVID-19 global pandemic, which has caused a reduction of economic activities worldwide.

Discussions

Origin of Tremor: Perspective, Interpretation & Outstanding Questions

In our study, we were able to associate only one of the tremor sequences to an event in the global catalog. Our attempt to associate the other events in the tremor sequences to either a previously undetected global or regional event proved inconclusive. This lack of corroborating seismic evidence confirming anecdotal reports could be due to either of the following: (1) the inaccuracy of the timing or the number of the reports, (2) localized low-magnitude shaking not detectable by the seismic station closest to Abuja, due to the quality of the data recovered from that seismic station (i.e. TORO). While this is an unsatisfactory conclusion, it emphasizes the need for high-quality data in regions that are often ignored due to the assumption of lack of seismicity. We also demonstrated that one of the reported tremor activities in Abuja, Nigeria, and recorded by the Western African stations, is coincident with the Hokkaido Eastern Iburi, Japanese earthquake of Sept 5. 2018. It is very puzzling that this moderate-sized earthquake (~M6.7) generated enough seismic energy to be felt in the capital city of Nigeria, considering that Japan is located at considerable teleseismic distances (~112 degrees). Here, we discuss a few plausible scenarios

that may offer more insights into these results taken together.

Hypothesis I: A Unique Teleseismic Event

While we are aware that a moderate teleseismic event is improbable to cause significant shaking at a considerable distance, it is tempting to explore the possibility that there is a direct connection to this event due to a large number of co-seismic landslides (Zhang et al., 2019) generated significant long-period surface wave energy that propagated to large distances without much dissipation (Allstadt, 2013). Landslides can be effectively modeled by single-forces, where the orientation of the force exerted on the earth is in the direction opposite landslide acceleration, generating maximum surface wave amplitudes along the trajectory of mass loss (Ekström et al., 2003; Kawakatsu, 1989; Tsai & Ekström, 2007). For shallow landslides with estimated mass volumes and a simple trajectory, it should be straightforward to model the effective forces, using synthetic seismograms (Ekström & Stark, 2013). However, the Hokkaido Iburi Earthquake triggered ~6,000 landslides with complex trajectories (Figure 8), distributed over a large area making this a difficult task. Despite this complexity, we observe that the aggregate spatial distribution of the landslides can explain surface-wave radiation in the direction of Nigeria (310 degrees, which is in the NW/SE direction from Japan) (Figure 8).

A comprehensive inventory of landslides (F. Wang et al., 2019; Zhang et al., 2019) document important characteristics that fit this pattern: a large concentration of 65% of the landslides (21 per square-km) in an elliptical area of 173 squared-km with major axis oriented NNW/SEE at 327.7 degrees (within 18 degrees of the direction of Abuja). We expect that a considerable portion of the radiated surface-wave energy is connected to the co-seismic landslides separate from the triggering earthquake, which has been modeled as a deep-crustal earthquake with different rupture process, and surface wave radiation patterns (Gou et al., 2019; Hua et al., 2019; Kobayashi et al., 2019; Zang et al., 2019). Although we report an event detection, we do not expect significant shaking from radiated energy from the landslide. It is more plausible that this event caused slight stress perturbations that reactivated local basement fractures (cite authors). We explore this hypothesis next.

Hypothesis II: Local Amplification of Earthquakes from Regional Tectonics

Previous studies have documented the occurrence of earthquakes in the Western African continental region and especially within continental Nigeria (Ajakaiye et al., 1987; Blundell, 1976; Scheidegger & Ajakaiye, 1985; Williams & Williams, 1977; Wright, 1976). These earthquakes have been attributed to (1) the inland continuation of oceanic fracture zones (Blundell, 1976; Wright, 1976) or (2) seismicity associated with faulting along the Cameroon volcanic line (Nfomou et al., 2004; Tabod et al., 1992). The apparent extension of the oceanic fracture zones across the continent-ocean boundary towards the shoreline in the Gulf of Guinea (Figure 1a; (Granot & Dyment, 2015)) may explain the clustering of historical seismicity close to the shorelines (Figure 1a), but may not explain the events reported from areas further inland. We note that historical tremors that were felt in the inland areas (north-central part of Nigeria) are distributed across both the failed rifts and

areas of the exposed basement on the rift flanks (figure 1a).

We consider an alternative hypothesis that the series of shakings felt in the study area (Abuja area, north-central Nigeria) may be related to the local amplification of possible earthquakes associated with the active tectonics along the offshore oceanic fracture zones (transforms), or along the active Cameroon Volcanic Line in the east. The Abuja area is located within the broad basement complex terrain of Nigeria (i.e., outboard of the Mesozoic failed rifts), where the basement rocks are dominated by Precambrian migmatite gneiss and granitic intrusions (Oyawoye, 1964). The granitic intrusions occur as prominent topographic-highs in the landscape, and the gneissic host rocks occur as topographic-lows where small basins of unconsolidated sediments commonly accumulate. Our estimation of basement undulations in the Abuja area shows that the locations where the tremor was felt are located within a small sedimentary basin (Figure 6g), indicating a vulnerability of the local geology of the Abuja area to seismic amplification. Although both the oceanic transforms and areas near the Cameroon Volcanic Line show seismic activity (Figure 1a), our catalog search did not identify any event along the offshore oceanic transforms or the Cameroon volcanic Line that coincides with the timing of the shaking.

Hypothesis III: Reactivation of Local Basement Fractures and Fault Systems by Post-Rift Crustal Relaxation or Far-field Tectonic Stresses

Although we report inconclusive evidence for an earthquake in Nigeria, we emphasize that the absence of evidence is not the evidence of absence, considering the poor data quality from the closest station (TORO). As mentioned earlier, the historical earthquakes in Nigeria have been attributed to the inland continuation of oceanic fracture zones through the Precambrian basement shear zones (Anifowose et al., 2006; Blundell, 1976; Odeyemi, 1989, 2006; Wright, 1976). However, these Precambrian basement shear zones (cyan dotted lines in Figure 1a) show a NNE trend that is markedly distinct from the ENE-to-NE trends of the oceanic fracture zones. Rather, the oceanic fracture zones show better spatial and azimuthal correlation with the NE-trending Benue Trough (failed Mesozoic rift) than the onshore basement shear zones (Figure 1a). In addition, there exists no surficial evidence of recent fault scarps or collocated active brittle exploitation along the trend of the basement shear zones. Therefore, we examine the brittle structures in the basement of the Abuja area which is located on the flank of the Benue Trough, with a view of possible local seismic reactivation of pre-existing basement fracture systems.

Our analysis of the exposed basement fracture systems (Figures 6a-c) and deeper structures of the aeromagnetic lineaments (Figures 6d-e) show common prominent sets of conjugate NE-SW and NW-SE trends. Thus, we interpret these structural trends to be the dominant patterns of the basement fracture systems and faults in the Abuja area. We note that the Abuja area is located near the nexus of two Mesozoic rift basins (failed rifts), the NW-trending Bida Basin and NE-trending Benue Trough (Figures 1a and 6c). The basins are composed of basement-rooting structures that are associated with the opening

(Mid-Cretaceous) and closing (Late Cretaceous) of the West and Central African Rift System. We find that the axial trends of these two rift structures are parallel to the most prominent structural trends in the Abuja area (Figure 6c). This suggests that the pre-existing discontinuities in the Abuja area are most-likely inherited from the Mesozoic extensional tectonic deformation. We propose that these basement structures may be reactivated either by far-field tectonic stresses or post-rift relaxation of the crust.

Unfortunately, there exists no published stress field data in the interior of Nigeria (Heidbach et al., 2018). Nevertheless, to provide a first-order assessment, we consider the closest available measurement of the in-situ azimuth of 176° for the maximum horizontal compressional stress (SHmax from borehole breakout) at a location in SW Nigeria (Figure 6c inset; (Heidbach et al., 2018)). If this available stress data is representative of the current $\sigma 1$ magnitude and orientation in the Abuja area, the NW-trending fractures are more critically oriented for reactivation (in strike-slip mode) than those in the NE and E-W trends. We recommend future studies to explore the in-situ stress field across the region in order to better understand the susceptibility of the inherited structures to seismic reactivation.

Based on the geological considerations presented above, we infer that in the Abuja area, there exist basement discontinuities that could be optimally-oriented for seismic reactivation by stress perturbation of the assumed current stress field. On a regional scale of the Western Africa sub-continent, we highlight the occurrence of earthquakes in the Mesozoic rift structures and the Precambrian basement domains (earthquakes in Termit Basin, Benue Trough, Yola-Doba Basin, Ahaggar Massif, and West African Craton in Figure 6a); suggesting that inherited brittle structures in the basement pose important seismic hazards across the region. Overall, we emphasize that the faults and fracture systems of the failed Mesozoic rift basins in the Westen Africa region (West African Rift System, Figure 1a) represent critical seismic hazards in the region that may be capable of hosting damaging earthquakes.

Hypothesis IV: Induced Earthquake Triggering by Groundwater Extraction

The widespread subsidence observed in the study area is consistent with those measured in other metro areas around the world and likely to be associated with fluid (primarily groundwater) extraction (Chaussard et al., 2014; Herrera-García et al., 2021; Megan Marie Miller et al., 2017; Megan M. Miller & Shirzaei, 2019; M. M. Miller & Shirzaei, 2015). A change in near-surface hydrologic loading has the potential to alter the local and regional stress field (Amos et al., 2014; Johnson et al., 2017a, 2017b, 2020), which can encourage earthquake nucleation and may weakly modulate seismicity (Heki, 2003; Johnson et al., 2017a). In regions where elastic loading maintains a strong periodic signal, the same cyclic pattern is observed in seismic catalogs (Ader & Avouac, 2013; Heki, 2003). Furthermore, stress and pressure in the crust can be altered due to fluid injection and extraction, triggering earthquakes (Ellsworth, 2013; Keranen & Weingarten, 2018; Kwiatek et al., 2019; Paul Segall, 2010; P. Segall & Lu, 2015; Manoochehr Shirzaei et al., 2016; H. F. Wang, 2001; R. Wang &

Kümpel, 2003; Zhai et al., 2019, 2021). The stress and pressure gain is a function of pumping and injection location, flux, and accumulated volume, while the rate of radial fluid migration is mainly controlled by crustal permeability (P. Segall & Lu, 2015; H. F. Wang, 2001).

Fault failure may occur when shear stress exceeds the fault shear strength for a given effective normal stress. Shear stress can be altered due to non-zero differential stress changes caused by the imparted stress. Also, effective normal stress depends on the magnitude of the stresses and the orientation of the fault in the tectonic stress field. The magnitude of fault-normal stresses can be reduced due to increased pore fluid pressure. However, establishing a threshold for stress and pressure change to trigger an earthquake is not trivial (e.g., (Talwani & Acree, 1985)). It is often assumed that faults are near critically stressed if they have not ruptured recently (Townend & Zoback, 2000). Therefore, a small perturbation of the stress field due to the loading effect and fluid diffusion may trigger some earthquakes. Some examples include seasonal modulation of seismicity due to hydrological loading cycles (Carlson et al., 2020; Christiansen et al., 2007; Johnson et al., 2017a), triggering earthquakes due to tides (Tanaka et al., 2002; Wilcock, 2001), and induced seismicity due to pore pressure change by seasonal precipitation or snowmelt (Hainzl et al., 2006; Montgomery−Brown et al., 2019; Saar & Manga, 2003) .

Despite scientific evidence from elsewhere, in the Abuja case study, investigating the hypothesis that the events similar to that of September 2018 are of hydrological origin is not straightforward due to the lack of dense hydrological observations (e.g., groundwater levels, stream discharge) and a complete seismic catalog. Therefore, we call for future efforts to generate new observations and develop models that constrain spatiotemporal variations in components of total water storage and establish a link to the local and regional tectonics and seismicity. Such data and models will further enhance the knowledge of water availability and improve the local communities' resilience to drought in the era of climate change.

Summary: Preferred Hypotheses and Strategies for Further Tests

Our exploration of the limited, yet very important geological and geophysical datasets have shed light on the most plausible cause of the shaking experienced in Abuja between Sept 5-7, 2018. Based on the available InSAR analysis, we find the strongest support for the hypotheses that these events were triggered by groundwater extraction (H-IV). Similarly, some recently published strain rate modelling from country-wide GNSS network covering the period of 2012 to 2015 (i.e. prior to the 2018 tremors; (Bawa et al., 2020)) shows a localized subsidence zone (negative dilation) that is collocated with a prominent subsidence zone in our analyses (see location b of Fig. 7a). This subsidence anomaly is located directly over the Jere Irrigation Project, which was reportedly active at the time of the reported tremors. Following closely, is the hypothesis that at least one of the felt events could have been triggered by the remote teleseismic event in Japan (H-I). While this idea is plausible, we have no actual data to confirm this hypothesis, because the closest seismic station did not

record good enough data to investigate this hypothesis any further (see examples (Han et al., 2017)). This again underscores the need for a high-quality geodetic and seismic network in the region. Similarly, a thorough examination of both hypotheses related to local fault reactivation by regional tectonics would require a high quality seismic and geodetic network to evaluate its plausibility for future events (H-II and III). All the evidence taken together, we point out that, although the Abuja area is located on a stable intraplate region within the continent, transient strain rates, e.g. recharge and discharge of aquifers, may be more important than the background tectonic strain rates when it comes to triggering an earthquake swarm (Calais et al., 2016; Gardonio et al., 2018; Sykes, 1978; Wolin et al., 2012). The Western African crystalline basement is dominated by inherited crustal weaknesses that may then fail due to this large transient stress release. Should such events reoccur in the future, further evaluation of our proposed hypotheses would definitely benefit from a renewed geophysical investigation of the Western African region, which is currently grossly understudied and poorly instrumented.

Conclusions

We investigated the source of ground shaking reported during Sept 5-7, 2018 in the Abuja area, central Nigeria. We reviewed previous seismic activity in the region, speculated on how the shaking is related to unique teleseismic events, or may be connected to other alternative explanations, i.e., anthropogenically triggered, or whether regional tectonics and local geology could have made the region more susceptible to triggered fault rupture and amplification of seismic shaking. We explored the spatial and temporal origins of the shaking using seismology, and studied the basement structure and surface deformation using aeromagnetic and SAR data. We found the strongest support for seismicity related to anthropogenic ground-water extraction. While other hypotheses cannot be ruled out completely for the case-study presented here, we point out that more work is needed to establish a better understanding of the potential connections between inherited basement structure, active regional tectonics, and anthropogenic stress perturbations.

Data and Resources

All the seismic data used in this study are publicly available through USGS and IRIS. The MATLAB code for polarization was originally developed by Matt Haney based on the covariance method and coherency method discussed by Vidale (1986). M_idist (T. Vincenty, 1975) is used to calculate the distance between the station and source location and the corresponding azimuth, and Matlab_TauP based on (Crotwell et al., 1999) is used to calculate the travel time of seismic phases given a list of event parameters (such as origins and magnitude). We use the irisFetch FDSN event web service method (irisFetch.Events) to retrieve seismic data.

Acknowledgments

The authors acknowledge the use of the BlueHive Linux cluster at the University of Rochester's center for integrated research computing - CIRC. Yingping Lu acknowledges a summer research grant from URSeismo and funding from the Georgen Institute of Data Science. We thank the Nigeria Geological Survey Agency (NGSA) for providing the aeromagnetic data used in this study. We acknowledge many helpful discussions with members of the URSeismo lab: Baowei Liu, Ziqi Zhang, Liam Moser, Trey Brink, and Faner Lin. We also thank the editor … and reviewers for their constructive comments. The facilities of IRIS Data Services, and specifically the IRIS Data Management Center, were used for access to waveforms, related metadata, and/or derived products used in this study. IRIS Data Services are funded through the Seismological Facilities for the Advancement of Geoscience (SAGE) Award of the National Science Foundation under Cooperative Service Agreement EAR-1851048. The satellite (Figure 6) and aeromagnetic data (Figure 8) used for this research are published on a public repository at (Olugboji, 2020) and included as google KMZ files in the supplementary information files - Datasets S1 and S2.

Appendix

Single-station earth-quake location

The primary goal of a single-station location using polarization analysis is to determine the epicenter of an earthquake source. We use a three-channel single-station recording to estimate the arrival azimuth, and station-earthquake epicentral distance (ϕ_{s-e}, Δ_{s-e}). This starts with phase identification, estimation of relative travel-time separation of the identified phases, and finally the estimation of the azimuth using either the compressional or the Rayleigh wave. Each phase can be detected using its polarization signature. We apply both the time and frequency-domain algorithms that have been developed for estimating the time-varying polarization properties of a signal. We form a $L \times 3$ matrix using the three-channel seismogram with the number of samples L:

$$\mathbf{X}(t) = [X_Z(t), X_N(t), X_E(t)]$$

we then compute the covariance matrix, $\mathbf{S}(t)$, which is used to obtain the direction of polarization, $\hat{\mathbf{U}}_j$, through singular value decomposition (SVD) (Jurkevics, 1988):

$$\mathbf{S}(t) = \frac{1}{L}\sum_{i=1}^{L} \mathbf{X(t)X^T(t)}$$

$$(\mathbf{S}(t) - \lambda_j \mathbf{I})\hat{\mathbf{U}}_j(t) = 0$$

We apply a moving-window smoothing filter of length l = L/10 to the matrix X before SVD. It is customary to sort the corresponding eigenvalues (λ_j) and their corresponding

eigenvectors from largest to smallest so that $\lambda_0 > \lambda_1 > \lambda_2$. In this ordering, the contribution of the dominant principal axes (eigenvector) of the estimated signal's particle motion, $\hat{\mathbf{U}}_0$ is then utilized to determine the azimuth, ϕ, and dip, ψ, of the incoming phase (see supplementary figure 1):

$$\hat{\mathbf{u}}_0(t) = [U_Z(t), U_N(t), U_E(t)]$$

$$\phi(t) = \arctan\left(\frac{U_E}{U_N}\right)$$

$$\psi(t) = \arctan\left(\frac{U_Z}{\sqrt{U_N^2 + U_E^2}}\right)$$

The detection of distinct phases: *P, SV,* Love or Rayleigh wave phases follow the identification of the appropriate combination of polarization parameters in the appropriate time window. The most important polarization parameter for robust body-wave phase detection is the strength of rectilinearity $f(\lambda_j)$ (Reading et al., 2001; Weber et al., 2011) which we obtain using the coherence technique (Vidale, 1986), after a slight modification to the covariance approach. The real signal $\mathbf{X}(t)$ is used to construct the complex analytical signal, $\widetilde{\mathbf{X}}(t)$:

$$\widetilde{\mathbf{X}}(t) = \mathbf{X}_r(t) + iH(\mathbf{X}_r(t))$$

where H is the Hilbert transform and i is the complex number $\sqrt{-1}$. In this form, the complex covariance matrix, and polarization directions are obtained from complex conjugation, $\mathbf{C}(t) = \widetilde{\mathbf{X}}(t)\widetilde{\mathbf{X}}^*(t)$ and replace the $\mathbf{S}(t)$ matrix. The complex polarization direction is then $\widetilde{\hat{\mathbf{U}}}_j(t)$ from which we can determine the strength of linear polarization:

$$f(\lambda_j, \hat{\mathbf{U}}_{0r}) = P_S - P_E$$

$$P_S = 1 - \frac{\lambda_1 + \lambda_2}{\lambda_0}$$

$$P_E = 1 - \frac{\sqrt{1 - \hat{\mathbf{U}}_{0r}^2}}{\hat{\mathbf{U}}_{0r}}$$

Where P_S and P_E are the strength of linear and elliptical polarization respectively. Since we use both the eigenvalues and the complex eigenvectors to determine the strength of linear

polarization, we need to maximize the real component of the largest eigenvectors in $\widetilde{\mathbf{U}}_0(t)$ derived from $\mathbf{C}(t)$.

The polarization time series is used to determine the arrival time of candidate *P* and *SV* phases, by combining into characteristic functions and defining empirical threshold values (Allen, 1982) which are resistant to false triggers (Bai & Kennett, 2000, 2001):

$$\mathbf{I^P}(t) = \mathbf{I_f^P} \otimes \mathbf{I_E^P} \oplus \mathbf{I}_\psi^\mathbf{P}$$

$$\mathbf{I^{SV}}(t) = \mathbf{I_f^{SV}} \otimes \mathbf{I_E^{SV}} \oplus \mathbf{I}_\psi^\mathbf{SV}$$

for surface waves (SW = Love or Rayleigh), detection is triggered by requiring linearity for Love waves, ellipticity for Rayleigh waves, and a stable azimuth/dip criterion (minimum $\psi' = \partial\psi/\partial t$):

$$\mathbf{I^{SW:L}} = \mathbf{I_f^{SW}} \otimes \mathbf{I}_{\psi'}^\mathbf{SW} \otimes \mathbf{I_E^{SW}} \ominus (\mathbf{I^P} \oplus \mathbf{I^{SV}})$$

$$\mathbf{I^{SW:R}} = \mathbf{I_{-f}^{SW}} \otimes \mathbf{I}_{\psi'}^\mathbf{SW} \otimes \mathbf{I_E^{SW}} \ominus (\mathbf{I^P} \oplus \mathbf{I^{SV}})$$

The logical operations $\otimes, \oplus, \ominus$ represent AND (intersection), OR(union), and NOT respectively, and each characteristic function is obtained from combining binary thresholding functions $\mathbf{I}_\chi$ applied to each polarization parameter: χ. The inclusion of an energy analysis $(\chi = \mathbf{E})$ incorporates the well-known short-term/long-term average of raw ground displacement before $(\mathbf{E_X})$ and after SVD $(\mathbf{E_U})$, which ensures that phase detection is triggered when the amplitude of the incoming phase is large relative to background noise (Allen, 1982; Astiz et al., 1996).

For example, for the *P* phase dip angle, $\chi = \psi$, and $\mathbf{I}_\psi^\mathbf{P}$ is the characteristic function of the dip-angle using a (de-)trigger threshold that correctly identifies the arrival time of the P-phase (see supplementary Figure 2) (Earle, 1999) .

$$\mathbf{I}_\psi^\mathbf{P}(t) = \begin{cases} 0 & \psi \le \psi_{p+} \\ 1 & \psi \ge \psi_{p+} \\ 0 & \psi \le \psi_{p-} \otimes I_\chi = 1 \end{cases}$$

For the definition of the other threshold functions, $\mathbf{I}_\chi$, and details of how the appropriate (de-) trigger thresholds are set, see supplementary table 2. Consult the supplementary information for a benchmark of the algorithm.

Tables

Table 1: (a) Stations used to discriminate local and teleseismic events originating from West-Africa. Stations G.TAM has only one horizontal channel, station II.ASCN is an island station and station PM.PFVI is located in Portugal, but with very little propagation in the Atlantic ocean. We include II.RAYN, which is a very quiet station, to broaden the back-azimuth coverage, even though it is technically in the Middle east. (b) Distance and azimuth estimation result from hypothesis-based statistics.

No.	Code	Country	Coordinates (Lat, Lon)	$X_{N\ angle}$ *	Location code
1	**II-RAYN**	**Saudi Arabia**	**23.5224, 45.5032**	**0 °**	**00**
2	**MN-WDD**	**Malta**	**35.8373, 14.5242**	**-3°**	**--**
3	**IU-FURI**	**Ethiopia**	**8.8952, 38.6798**	**-1°**	**00**
4	PM-PFVI	Portugal	37.1328, -8.8268	6°	--
5	G-TAM	Algeria	22.7915, 5.5284	2°	00
6	**II-MBAR**	**Uganda**	**-0.6019, 30.7382**	**0°**	**00**
7	NJ-TORO	Nigeria	10.055, 9.12	6°	--
8	G-MBO	Senegal	14.392, -16.9555	-8°	10
9	**GT-DBIC**	**Cote d'Ivoire**	**6.6702, -4.8566**	**15°**	**00**
10	II-ASCN	Ascension Island	-7.9327, -14.3601	-1°	00

*Proper orientation for North channel is retrieved from (Ojo et al., 2019).

H_0: Regional event with epicenter in Nigeria.

H_1: Teleseismic event with epicenter in Japan.

No.	$\Delta^{0,1}$	ΔH_0	ΔH_1	Φ^0	ΦH_0	ΦH_1	$\varepsilon\Delta H_0$	$\varepsilon\Delta H_1$	$\varepsilon\Phi H_0$	$\varepsilon\Phi H_1$
1	**85°**	**38°**	**79°**	**226°**	**63°**	**292°**	**123%**	**8%**	**258%**	**22%**
2	**86°**	**27°**	**88°**	**300°**	**10°**	**320°**	**218%**	**2%**	**2771%**	**6%**
3	**85°**	**30°**	**94°**	**294°**	**88°**	**286°**	**187%**	**9%**	**234%**	**3%**
6	**101°**	**24°**	**106°**	**272°**	**112°**	**284°**	**320%**	**5%**	**141%**	**5%**
9	**151°**	**14°**	**122°**	**270°**	**261°**	**320°**	**1007%**	**23%**	**4%**	**16%**

Figures and Captions

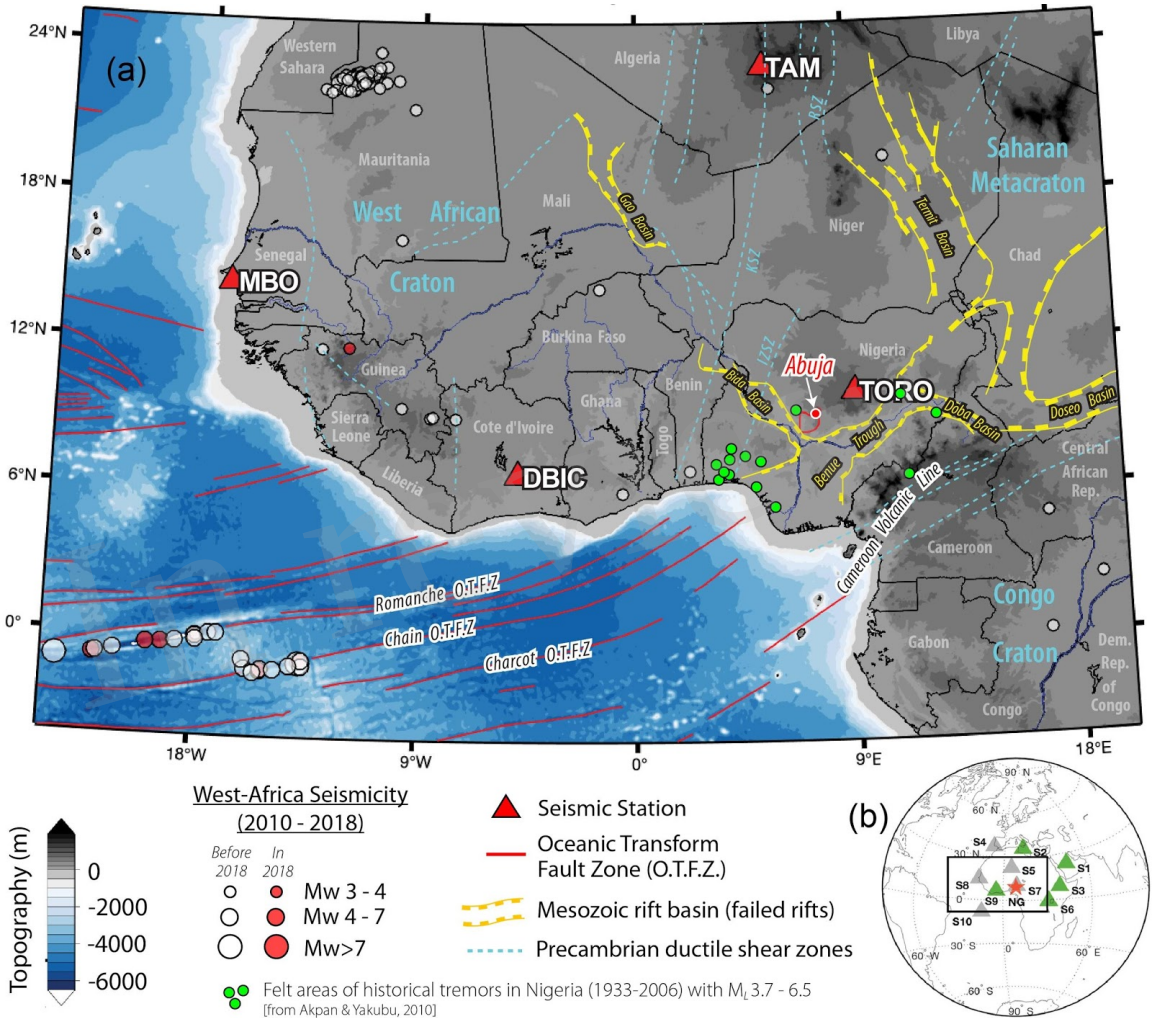

Figure 1. (a) West African seismicity and tectonics, showing the epicenters (circles) for earthquakes in the past decade with M3.0 and greater, ocean fracture zones (red lines), and the seismic network (triangles) available for seismic detection. The 2018 earthquake events (red circles) are outside the Abuja area (red polygon north-east of TORO). OTFZ = Oceanic Transform Fault Zone (oceanic fracture zone). Tectonic structures are from (Pérez-Díaz & Eagles, 2014) . The Mesosoic failed rifts shown in yellow lines define the West African Rift System. (b) Final selection of five stations (green triangle) used to search for an earthquake with a hypothetical epicenter (red star) located in Nigeria (NG). Grey stations do not pass the data quality selection criteria. Note that although TAM (S5) has good quality data, it is not used for single station detection since it only has one horizontal channel operating during the time of interest.

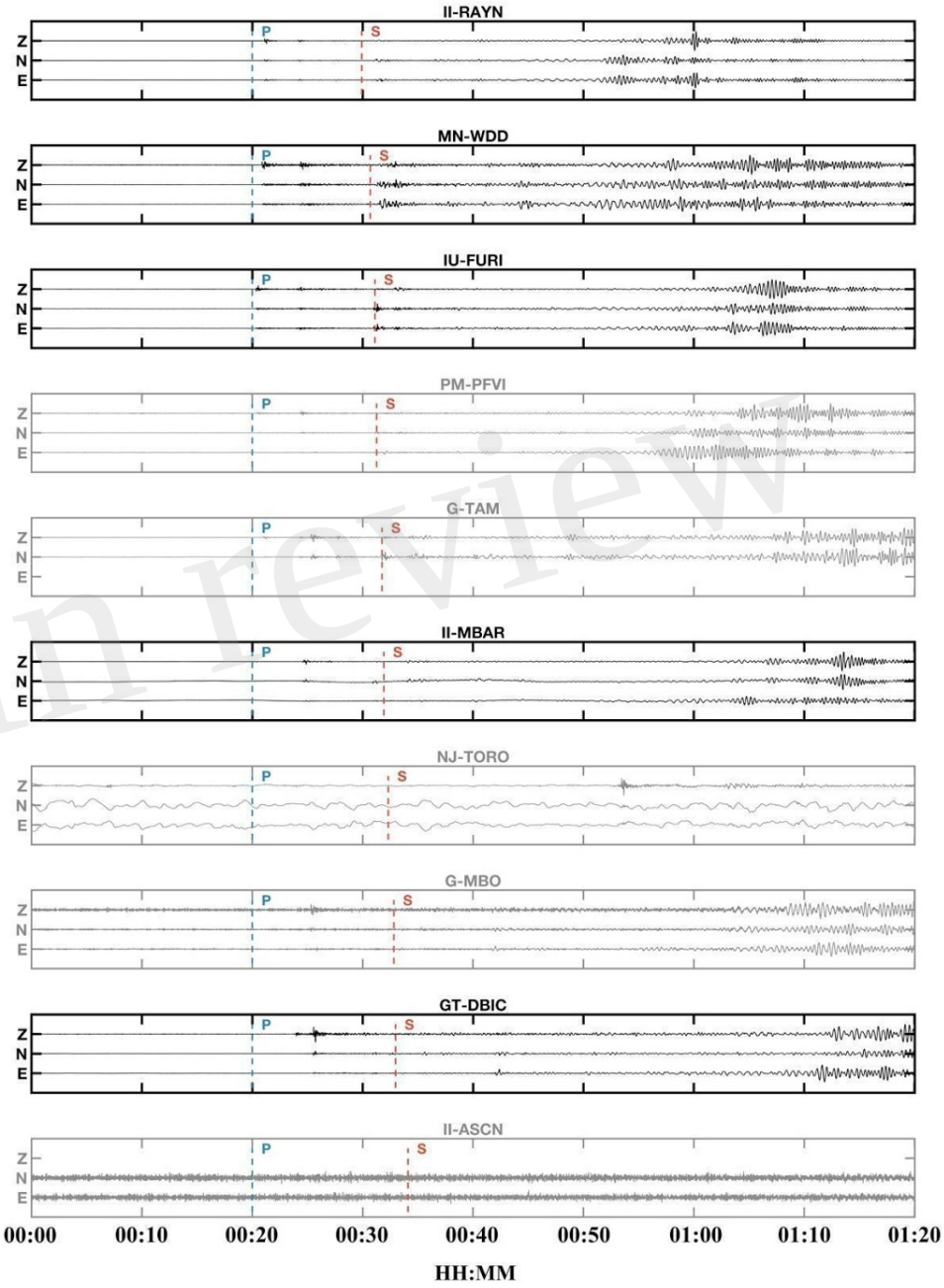

Figure 2. Seismograms at stations in or close to Nigeria using an 80-minutes time window. Traces are amplitude normalized. Stations used for further analysis, marked in black, are those that pass the data selection criteria (green triangles in Figure 1b). In each trace, the first P (blue) and S (red) arrivals of the M6.6 Hokkaido event are shown with the station code to the top.

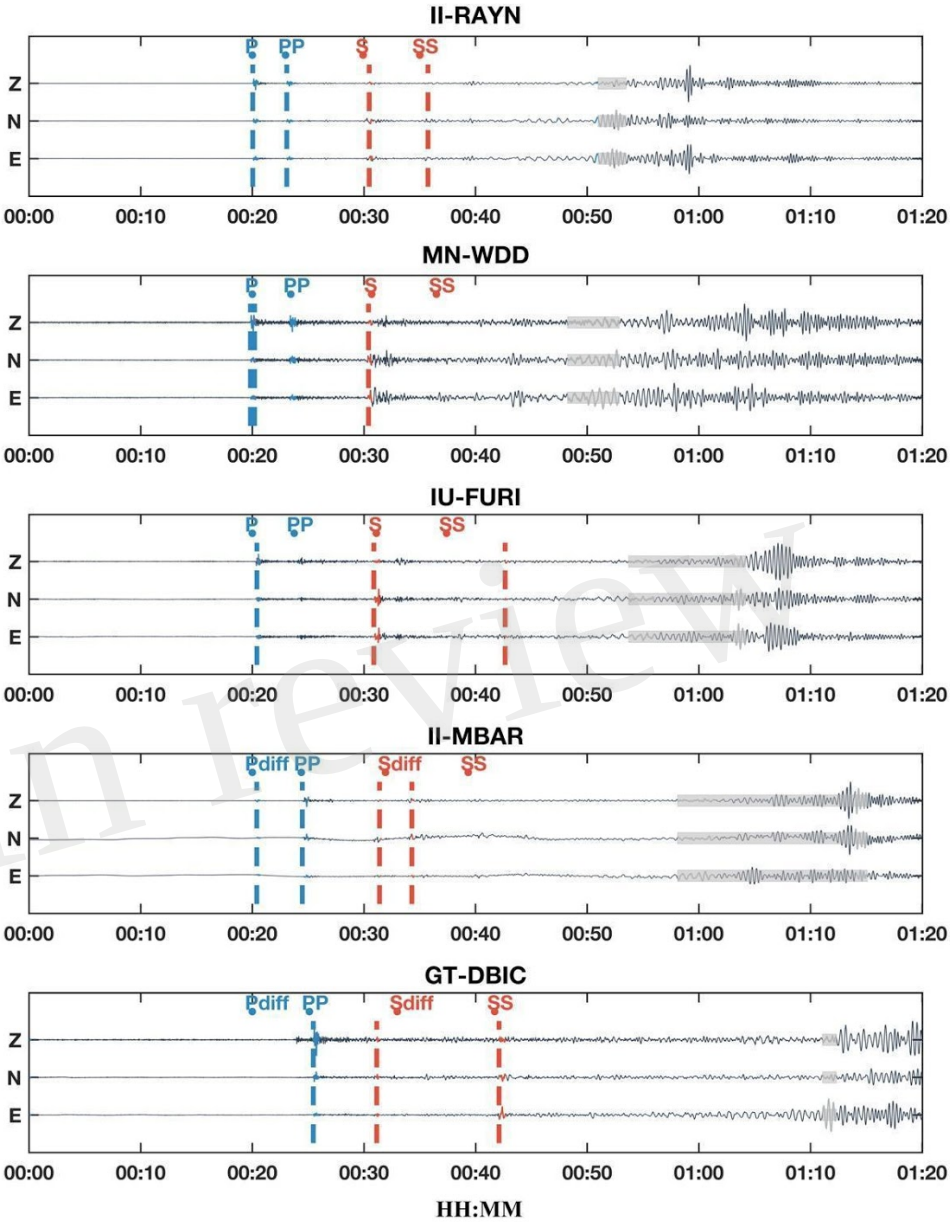

Figure 3. Phase detection using polarization analysis applied to data recorded at the five high-quality stations during the Hokkaido event of Sept. 5, 2018. The waveforms are for an 80-minute-long time window, where time 0:00 is 20 minutes before the P arrival at each station following the event origin. The detected arrival of P, S waves are marked with blue and red dashed lines, respectively, while the first arriving linearly polarized surface wave is shaded in grey. The predicted arrival time calculated using the earthquake parameters, and an earth model are indicated with dots and labels indicating the phase.

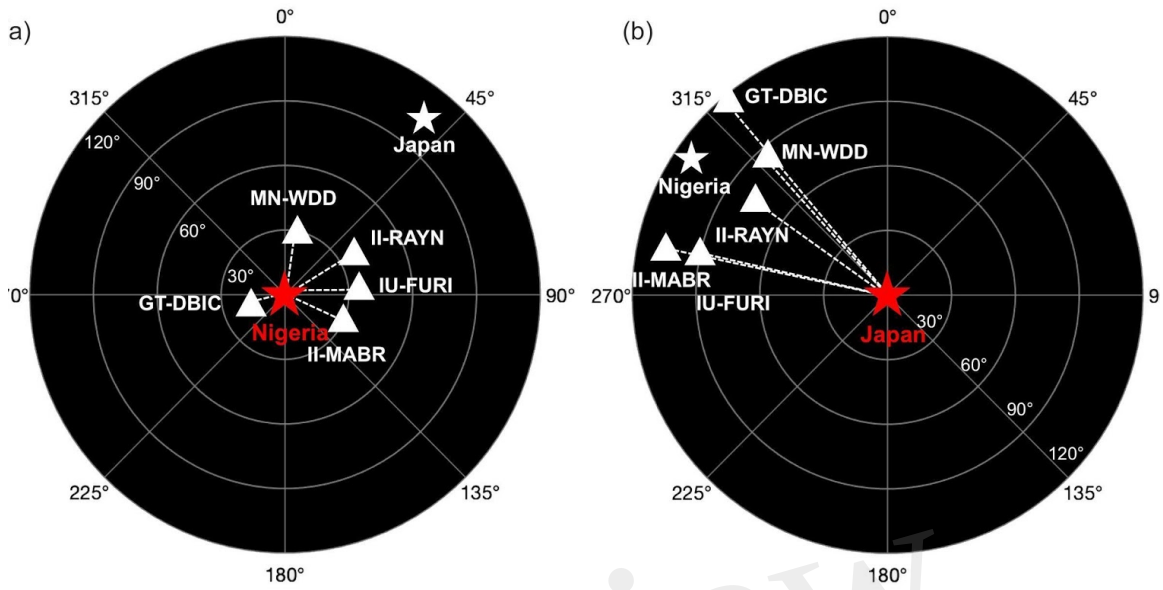

Figure 4. Station locations relative to two hypothetical epicenters (star). (a) For a local or regional event originating from Nigeria or within Western Africa, all stations are expected to be within 30 degrees of the event location (red star). (b) For the Hokkaido event, distance is $60 - 120°$ and azimuth $270 - 320°$ (compare Figure 5)

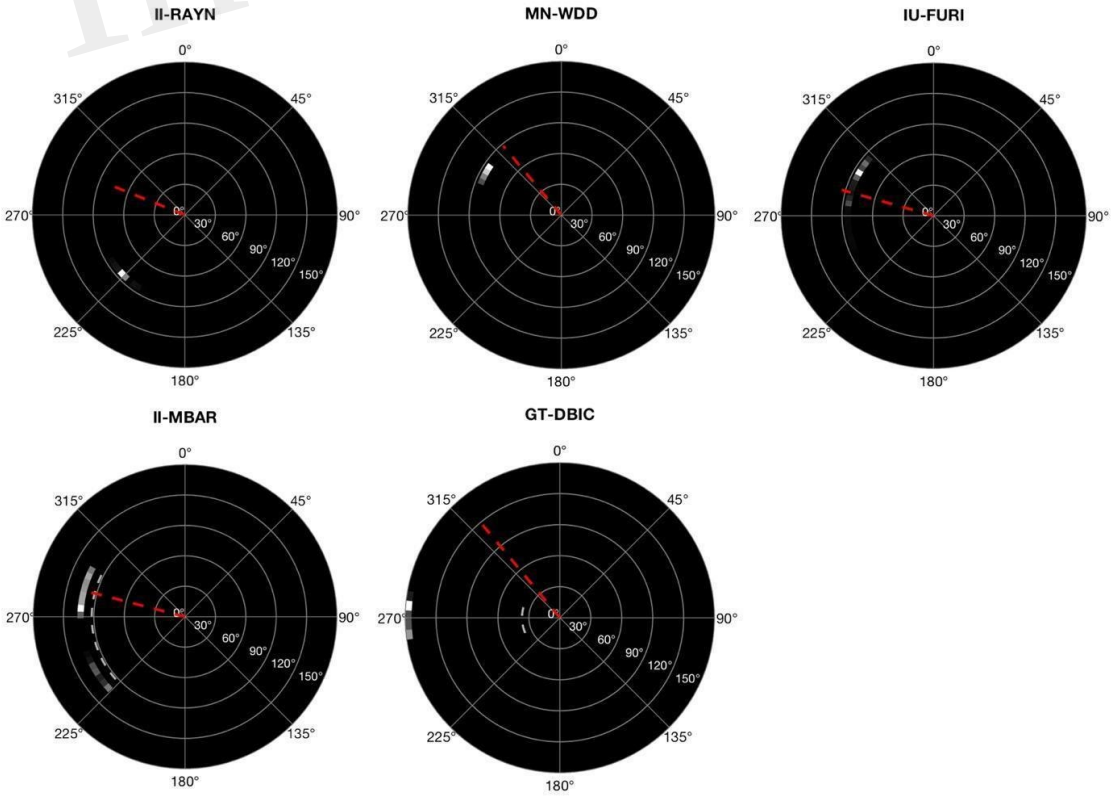

Figure 5: Single-station location of Hokkaido, Japan in the event reference frame (compare with station-event geometry in Figures 1b). All stations identify the correct epicentral distance and azimuth range (except for DBIC and RAYN with an azimuth bias of $-50°$).

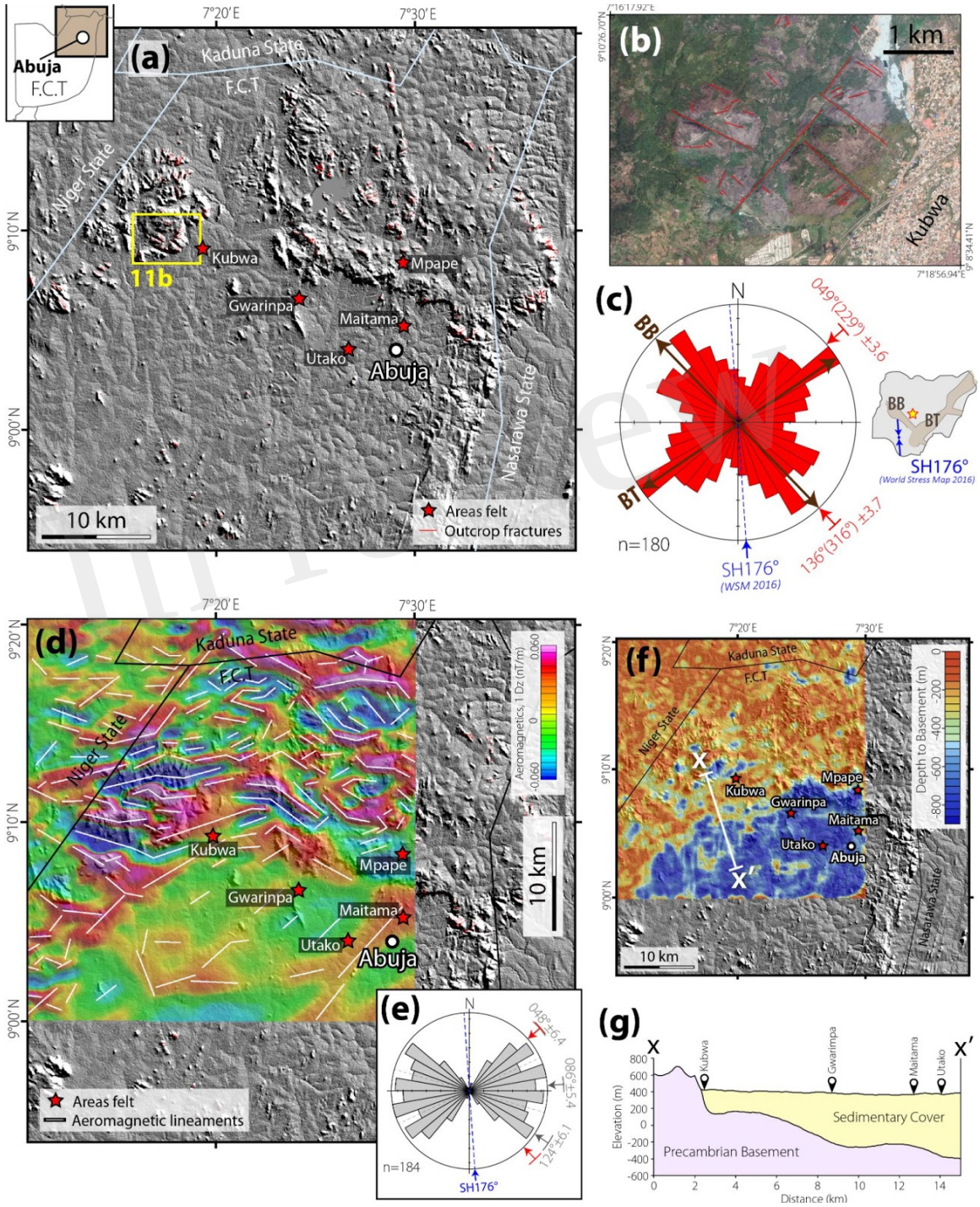

Figure 6: (a) Satellite topography hillshade map of the Abuja area of the Federal Capital Territory (F.C.T.), Nigeria, showing areas where the tremor was felt (source: BBC Africa Hausa). (b) Google Earth© satellite image of a part of the Abuja area showing an example of

satellite-scale fractures in the granitic basement outcrops. (c) Rose diagram showing the azimuth-frequency distribution of the satellite-scale outcrop fractures in the entire Abuja area shown in Figure 6a. SH=maximum horizontal compressional stress orientation (source: Heidbach et al., 2016). Inset: Map of Nigeria showing the location and orientation of SH data (Blue arrows), location of Abuja (red-yellow star), and Mesozoic rift basins (BT = Benue Trough, BB = Bida Basin). (d) The vertical derivative of the reduced to the equator (RTE) aeromagnetic map of the Abuja area. White lines represent the trends of basement magnetic anomaly lineaments. For 'SH', see 6c. (e) Rose diagram showing the azimuth-frequency distribution of the aeromagnetic lineaments, which represent the subsurface structural fabrics. The mean trends of the NW and NE dominant sets coincide considerably well with those of the satellite-scale outcrop fractures. (f) Depth to basement map, generated from the Source Parameter Imaging (SPI) transform of the aeromagnetic data, and the associated (g) cross-section, showing that the areas where the tremor was felt are located within a small sedimentary basin.

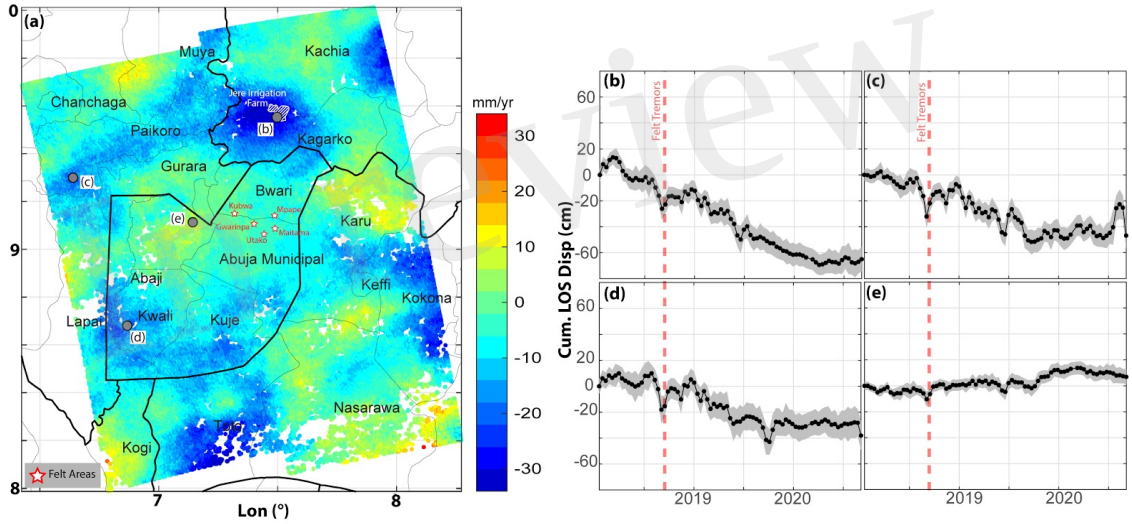

Figure 7. InSAR deformation map obtained from Sentinel-1A/B ascending orbit (heading ~347° and incidence angle ~38.5°) SAR images for period 2018/01/19-2020/09/05. (a) LOS linear velocity. Colder colors indicate movement away from satellite or subsidence. Black polygons show administrative divisions. (b)-(d) time series of LOS displacement at four locations shown in panel (a). The gray shading indicates a 1-sigma uncertainty range for the estimated time series.

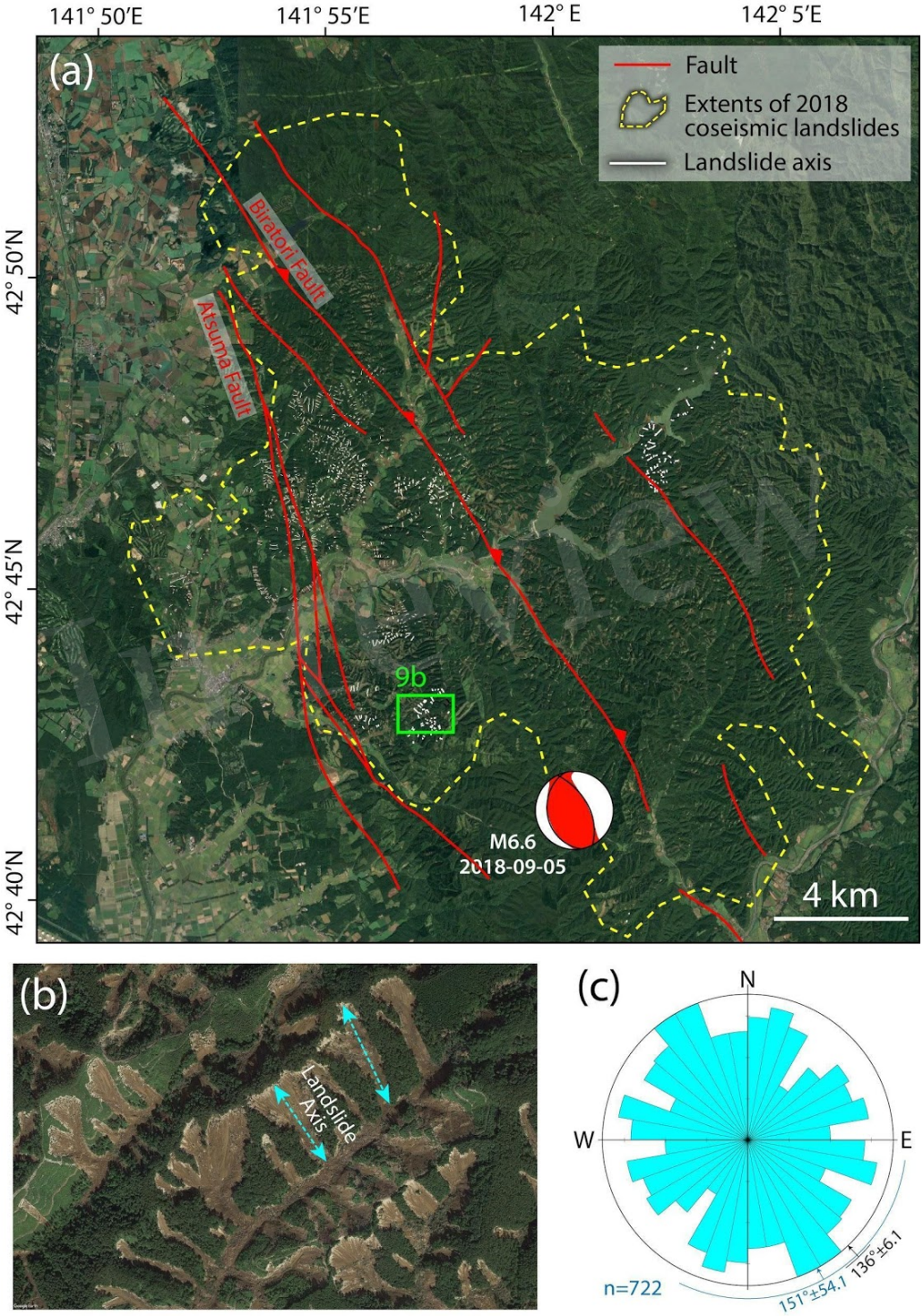

Figure 8: (a) Google Earth© satellite image of the Hokkaido landslide region showing the 270 km^2 extent of coverage of the affected area. (b) A representative satellite image showing the distribution of the individual landslides and the manually digitized axial trends (long-axes) of the landslides (see dataset S1 for digitized data). (c) Azimuth-frequency distribution of the mapped axial trends of the coseismic landslides.

References

Ader, T. J., & Avouac, J.-P. (2013). Detecting periodicities and declustering in earthquake catalogs using the Schuster spectrum, application to Himalayan seismicity. *Earth and Planetary Science Letters*, *377-378*, 97–105. https://doi.org/10.1016/j.epsl.2013.06.032

Afegbua, K. U., Abubakar, Y. T., & Umo, A. O. (2011). Towards an integrated seismic hazard monitoring in Nigeria using geophysical and geodetic techniques. *Journal of Physical* …. Retrieved from https://www.researchgate.net/profile/Umar_Kadiri/publication/267250110_Towards_an_integrated_seismic_hazard_monitoring_in_Nigeria_using_geophysical_and_geodetic_techniques/links/5c2bdbd2a6fdccfc7076f3f2/Towards-an-integrated-seismic-hazard-monitoring-in-Nigeria-using-geophysical-and-geodetic-techniques.pdf

Afegbua, K. U., Abubakar, Y. T., Umo, A. O., Dauda, D., & Saturday, U. E. (2011). Towards an integrated seismic hazard monitoring in Nigeria using geophysical and geodetic techniques. *International Journal of Physical Sciences*, *6*(28), 6385–6393. Retrieved from http://www.academicjournals.org/app/webroot/article/article1380626745_Afegbua%20et%20al.pdf

Afegbua, K. U., Ezomo, F. O., Osahon, O. D., Yakubu, T. A., & Sanni, H. T. (2019). Probabilistic seismic hazard assessment for national planning and development in Nigeria. *Journal of Geodynamics*, *126*, 46–55. https://doi.org/10.1016/j.jog.2019.03.004

Agius, M. R., & Galea, P. (2011). A Single-Station Automated Earthquake Location System at Wied Dalam Station, Malta. *Seismological Research Letters*, *82*(4), 545–559. https://doi.org/10.1785/gssrl.82.4.545

Ahulu, S., & Danuor, S. K. (2015). Ghana's experience in the establishment of a national digital seismic network observatory. *Journal of Seismology*, *19*(3), 667–683. Retrieved from https://link.springer.com/article/10.1007/s10950-015-9486-z

Ajakaiye, D. E., Daniyan, M. A., Ojo, S. B., & Onuoha, K. M. (1987). The July 28, 1984 southwestern Nigeria earthquake and its implications for the understanding of the tectonic structure of Nigeria. *Journal of Geodynamics*, *7*(3), 205–214. https://doi.org/10.1016/0264-3707(87)90005-6

Akpan, O. U., & Yakubu, T. A. (2010). A review of earthquake occurrences and observations in Nigeria. *Earthquake Science*, *23*(3), 289–294. https://doi.org/10.1007/s11589-010-0725-7

Akpan, O. U., Isogun, M. A., Yakubu, T. A., Adepelumi, A. A., Okereke, C. S., Oniku, A. S., & Oden, M. I. (2014). An evaluation of the 11th September, 2009 earthquake and its implication for understanding the Seismotectonics of south western Nigeria. *Open Journal of Geology*, *4*(10), 542. Retrieved from http://file.scirp.org/pdf/OJG_2014102914214509.pdf

Alaneme, K. K., & Okotete, E. A. (2018). Critical evaluation of seismic activities in Africa and curtailment policies – a review. *Geoenvironmental Disasters*, *5*(1), 24. https://doi.org/10.1186/s40677-018-0116-2

Allen, R. (1982). Automatic phase pickers: Their present use and future prospects. *Bulletin of the Seismological Society of America*, *72*(6B), S225–S242. Retrieved from https://pubs.geoscienceworld.org/ssa/bssa/article/72/6B/S225/102172/automatic-phase-pickers-their-present-use-and

Allstadt, K. (2013). Extracting source characteristics and dynamics of the August 2010 Mount Meager landslide from broadband seismograms. *Journal of Geophysical Research: Earth Surface*, *118*(3), 1472–1490. Retrieved from https://agupubs.onlinelibrary.wiley.com/doi/abs/10.1002/jgrf.20110

Amos, C. B., Audet, P., Hammond, W. C., Bürgmann, R., Johanson, I. A., & Blewitt, G. (2014). Uplift and seismicity driven by groundwater depletion in central California. *Nature*, *509*(7501), 483–486. https://doi.org/10.1038/nature13275

Anifowose, A. Y. B., Odeyemi, I. B., & Borode, A. M. (2006). The tectonic significance of the Ifewara-Zungeru megastructure in Nigeria. In *Teme SC and Ezeigbo C U. Proceedings of the 1st International Workshop on Geodesy and Geodynamics. Centre for Geodesy and Geodynamics, Toro, Nigeria* (Vol. 1728).

Astiz, L., Earle, P., & Shearer, P. (1996). Global Stacking of Broadband Seismograms. *Seismological Research Letters*, *67*(4), 8–18. https://doi.org/10.1785/gssrl.67.4.8

Bai, C.-Y., & Kennett, B. L. N. (2000). Automatic Phase-Detection and Identification by Full Use of a Single Three-Component Broadband Seismogram. *Bulletin of the Seismological Society of America*, *90*(1), 187–198. https://doi.org/10.1785/0119990070

Bai, C.-Y., & Kennett, B. L. N. (2001). Phase identification and attribute analysis of broadband seismograms at far-regional distances. *Journal of Seismology*, *5*(2), 217–231. https://doi.org/10.1023/A:1011436421196

Bawa, S., Ojigi, L. M., Dodo, J. D., & Lawal, K. M. (2020). Strain rate field on the Nigeria lithosphere derived from GNSS velocity. *Applied Geomatics*. https://doi.org/10.1007/s12518-020-00336-1

Blundell, D. J. (1976). Active faults in West Africa. *Earth and Planetary Science Letters*, *31*(2), 287–290. https://doi.org/10.1016/0012-821X(76)90221-1

Böse, M., Clinton, J. F., Ceylan, S., Euchner, F., van Driel, M., Khan, A., et al. (2017). A probabilistic framework for single-station location of seismicity on Earth and Mars. *Physics of the Earth and Planetary Interiors*, *262*, 48–65. https://doi.org/10.1016/j.pepi.2016.11.003

Calais, E., Camelbeeck, T., Stein, S., Liu, M., & Craig, T. J. (2016). A new paradigm for large earthquakes in stable continental plate interiors: LARGE EARTHQUAKES IN SCRs. *Geophysical Research Letters*, *43*(20), 10,621–10,637. https://doi.org/10.1002/2016gl070815

Carlson, G., Shirzaei, M., Werth, S., Zhai, G., & Ojha, C. (2020). Seasonal and Long−Term Groundwater Unloading in the Central Valley Modifies Crustal Stress. *Journal of Geophysical Research, [Solid Earth]*, *125*(1), 439. https://doi.org/10.1029/2019JB018490

Chaussard, E., Bürgmann, R., Shirzaei, M., Fielding, E. J., & Baker, B. (2014). Predictability of hydraulic head changes and basin-wide aquifer and fault characterization from InSAR-derived ground deformation. *Journal of Geophysical Research, [Solid Earth]*, *119*, 6572–6590.

Christiansen, L. B., Hurwitz, S., & Ingebritsen, S. E. (2007). Annual modulation of seismicity along the San Andreas Fault near Parkfield, CA. *Geophysical Research Letters*, *34*(4). https://doi.org/10.1029/2006gl028634

Crotwell, H. P., Owens, T. J., & Ritsema, J. (1999). The TauP Toolkit: Flexible seismic travel-time and ray-path utilities. *Seismological Research Letters*, *70*(c), 154–160. Retrieved from http://www.seis.sc.edu/downloads/TauP/taup.pdf

Doran, A. K., & Laske, G. (2017). Ocean−Bottom Seismometer Instrument Orientations via Automated Rayleigh−Wave Arrival−Angle MeasurementsOcean−Bottom Seismometer Instrument Orientations via Automated Rayleigh−Wave Arrival−Angle Measurements. *Bulletin of the Seismological Society of America*, *107*(2), 691–708. https://doi.org/10.1785/0120160165

Earle, P. S. (1999). Polarization of the Earth's teleseismic wavefield. *Geophysical Journal International*, *139*(1), 1–8. Retrieved from https://academic.oup.com/gji/article-abstract/139/1/1/574570

Ekström, G. (2006). Global detection and location of seismic sources by using surface waves. *Bulletin of the Seismological Society of America*, *96*(4), 1201–1212. https://doi.org/10.1785/0120050175

Ekström, G., & Stark, C. P. (2013). Simple scaling of catastrophic landslide dynamics. *Science*, *339*(6126), 1416–1419. https://doi.org/10.1126/science.1232887

Ekström, G., Nettles, M., & Abers, G. A. (2003). Glacial earthquakes. *Science*, *302*(5645), 622–624.

https://doi.org/10.1126/science.1088057

Ellsworth, W. L. (2013). Injection-induced earthquakes. *Science*, *341*(6142), 1225942. https://doi.org/10.1126/science.1225942

Farr, T. G., Rosen, P. A., Caro, E., Crippen, R., Duren, R., Hensley, S., et al. (2007). The shuttle radar topography mission. *Reviews of Geophysics* , *45*(2). https://doi.org/10.1029/2005rg000183

Franceschetti, G., & Lanari, R. (2018). Synthetic Aperture Radar Interferometry*. *Synthetic Aperture Radar Processing*. https://doi.org/10.1201/9780203737484-4

Frohlich, C., & Pulliam, J. (1999). Single-station location of seismic events: a review and a plea for more research. *Physics of the Earth and Planetary Interiors*, *113*(1), 277–291. https://doi.org/10.1016/S0031-9201(99)00055-2

Gardonio, B., Jolivet, R., Calais, E., & Leclère, H. (2018). The April 2017 M w 6.5 Botswana Earthquake: An Intraplate Event Triggered by Deep Fluids. *Geophysical Research Letters*, *45*(17), 8886–8896. https://doi.org/10.1029/2018GL078297

Gou, T., Huang, Z., Zhao, D., & Wang, L. (2019). Structural Heterogeneity and Anisotropy in the Source Zone of the 2018 Eastern Iburi Earthquake in Hokkaido, Japan. *Journal of Geophysical Research, [Solid Earth]*, *124*(7), 7052–7066. https://doi.org/10.1029/2019JB017388

Government Report. (2018, September 7). Retrieved January 14, 2020, from https://www.minesandsteel.gov.ng/wp-content/uploads/2018/09/Mpape-Tremor.pdf

Granot, R., & Dyment, J. (2015). The Cretaceous opening of the South Atlantic Ocean. *Earth and Planetary Science Letters*, *414*, 156–163. https://doi.org/10.1016/j.epsl.2015.01.015

Grauch, V. J. S., & Hudson, M. R. (2007). Guides to understanding the aeromagnetic expression of faults in sedimentary basins: Lessons learned from the central Rio Grande rift, New Mexico. *Geosphere*, *3*(6), 596–623. https://doi.org/10.1130/GES00128.1

Hainzl, S., Kraft, T., Wassermann, J., Igel, H., & Schmedes, E. (2006). Evidence for rainfall-triggered earthquake activity. *Geophysical Research Letters*, *33*(19). https://doi.org/10.1029/2006gl027642

Han, L., Peng, Z., Johnson, C. W., Pollitz, F. F., Li, L., Wang, B., et al. (2017). Shallow microearthquakes near Chongqing, China triggered by the Rayleigh waves of the 2015 M7.8 Gorkha, Nepal earthquake. *Earth and Planetary Science Letters*, *479*, 231–240. https://doi.org/10.1016/j.epsl.2017.09.024

Heidbach, O., Rajabi, M., Cui, X., Fuchs, K., Müller, B., Reinecker, J., et al. (2018). The World Stress Map database release 2016: Crustal stress pattern across scales. *Tectonophysics*, *744*, 484–498. https://doi.org/10.1016/j.tecto.2018.07.007

Heki, K. (2003). Snow load and seasonal variation of earthquake occurrence in Japan. *Earth and Planetary Science Letters*, *207*(1), 159–164. https://doi.org/10.1016/S0012-821X(02)01148-2

Herrera-García, G., Ezquerro, P., Tomás, R., Béjar-Pizarro, M., López-Vinielles, J., Rossi, M., et al. (2021). Mapping the global threat of land subsidence. *Science*, *371*(6524), 34–36. https://doi.org/10.1126/science.abb8549

Hua, Y., Zhao, D., Xu, Y., & Wang, Z. (2019). Arc-arc collision caused the 2018 Eastern Iburi earthquake (M 6.7) in Hokkaido, Japan. *Scientific Reports*, *9*(1), 13914. https://doi.org/10.1038/s41598-019-50305-x

Johnson, C. W., Fu, Y., & Bürgmann, R. (2017a). Seasonal water storage, stress modulation, and California seismicity. *Science*, *356*(6343), 1161–1164. https://doi.org/10.1126/science.aak9547

Johnson, C. W., Fu, Y., & Bürgmann, R. (2017b). Stress Models of the Annual Hydrospheric, Atmospheric, Thermal, and Tidal Loading Cycles on California Faults: Perturbation of Background Stress and Changes in Seismicity. *Journal of Geophysical Research: Solid Earth*. https://doi.org/10.1002/2017jb014778

Johnson, C. W., Fu, Y., & Bürgmann, R. (2020). Hydrospheric modulation of stress and seismicity on shallow faults in southern Alaska. *Earth and Planetary Science Letters*, *530*, 115904. https://doi.org/10.1016/j.epsl.2019.115904

Jurkevics, B. Y. A. (1988). POLARIZATION ANALYSIS OF THREE-COMPONENT ARRAY DATA. *Bulletin of the Seismological Society of America*, *78*(5), 1725–1743. Retrieved from http://citeseerx.ist.psu.edu/viewdoc/download?doi=10.1.1.472.9669&rep=rep1&type=pdf

Kameda, J., Kamiya, H., Masumoto, H., Morisaki, T., Hiratsuka, T., & Inaoi, C. (2019). Fluidized landslides triggered by the liquefaction of subsurface volcanic deposits during the 2018 Iburi-Tobu earthquake, Hokkaido. *Scientific Reports*, *9*(1), 13119. https://doi.org/10.1038/s41598-019-48820-y

Kawakatsu, H. (1989). Centroid single force inversion of seismic waves generated by landslides. *Journal of Geophysical Research*, *94*(B9), 12363. https://doi.org/10.1029/JB094iB09p12363

Keranen, K. M., & Weingarten, M. (2018). Induced Seismicity. *Annual Review of Earth and Planetary Sciences*, *46*(1), 149–174. https://doi.org/10.1146/annurev-earth-082517-010054

Kobayashi, T., Hayashi, K., & Yarai, H. (2019). Geodetically estimated location and geometry of the fault plane involved in the 2018 Hokkaido Eastern Iburi earthquake. *Earth, Planets and Space*, *71*(1), 62. https://doi.org/10.1186/s40623-019-1042-6

Kolawole, F., Atekwana, E. A., Laó-Dávila, D. A., Abdelsalam, M. G., Chindandali, P. R., Salima, J., & Kalindekafe, L. (2018). Active Deformation of Malawi Rift's North Basin Hinge Zone Modulated by Reactivation of Preexisting Precambrian Shear Zone Fabric. *Tectonics*, *37*, 683–704. https://doi.org/10.1002/2017TC004628

Kolawole, F., Johnston, C. S., Morgan, C. B., Chang, J. C., Marfurt, K. J., Lockner, D. A., et al. (2019). The susceptibility of Oklahoma's basement to seismic reactivation. *Nature Geoscience*, *12*(10), 839–844. https://doi.org/10.1038/s41561-019-0440-5

Koper, K. D., & Hawley, V. L. (2010). Frequency dependent polarization analysis of ambient seismic noise recorded at a broadband seismometer in the central United States. *Earthquake Science*, *23*(5), 439–447. https://doi.org/10.1007/s11589-010-0743-5

Kwiatek, G., Saarno, T., Ader, T., Bluemle, F., Bohnhoff, M., Chendorain, M., et al. (2019). Controlling fluid-induced seismicity during a 6.1-km-deep geothermal stimulation in Finland. *Science Advances*, *5*(5), eaav7224. https://doi.org/10.1126/sciadv.aav7224

Lay, T., Berger, J., Buland, R., Butler, R., Ekström, G., Hutt, C. R., & Romanowicz, B. (2002). Global seismic network design goals update 2002. *IRIS, August*, *26*. Retrieved from http://academic.aua.am/yelena_vardanyan/Web/flesh/Y/seis.pdf

Li, Y., & Oldenburg, D. W. (2001). Stable reduction to the pole at the magnetic equator. *Geophysics*, *66*(2), 571–578. https://doi.org/10.1190/1.1444948

Magotra, N., Ahmed, N., & Chael, E. (1987). Seismic event detection and source location using single-station (three-component) data. *Bulletin of the Seismological Society of America*, *77*(3), 958–971. Retrieved from https://pubs.geoscienceworld.org/ssa/bssa/article/77/3/958/118976/seismic-event-detection-and-source-location-using

Magotra, N., Ahmed, N., & Chael, E. (1989). Single-station seismic event detection and location. *IEEE Transactions on Geoscience and Remote Sensing: A Publication of the IEEE Geoscience and Remote Sensing Society*, *27*(1), 15–23. https://doi.org/10.1109/36.20270

Miller, M. M., & Shirzaei, M. (2015). Spatiotemporal characterization of land subsidence and uplift in Phoenix using InSAR time series and wavelet transforms. *Journal of Geophysical Research, [Solid Earth]*. Retrieved from https://agupubs.onlinelibrary.wiley.com/doi/abs/10.1002/2015JB012017

Miller, M. M., & Shirzaei, M. (2019). Land subsidence in Houston correlated with flooding from Hurricane Harvey. *Remote Sensing of*

Environment, *225*, 368–378. https://doi.org/10.1016/j.rse.2019.03.022

Miller, M. M., Shirzaei, M., & Argus, D. (2017). Aquifer mechanical properties and decelerated compaction in Tucson, Arizona. *Journal of Geophysical Research, [Solid Earth]*, *122*(10), 8402–8416. https://doi.org/10.1002/2017jb014531

Montgomery−Brown, E. K., Shelly, D. R., & Hsieh, P. A. (2019). Snowmelt−triggered earthquake swarms at the margin of Long Valley caldera, California. *Geophysical Research Letters*, *46*(7), 3698–3705. https://doi.org/10.1029/2019gl082254

Nakata, N., Gualtieri, L., & Fichtner, A. (2019). *Seismic Ambient Noise*. Cambridge University Press. Retrieved from https://play.google.com/store/books/details?id=o3uIDwAAQBAJ

Neves, M., Custódio, S., Peng, Z., & Ayorinde, A. (2018). Earthquake triggering in southeast Africa following the 2012 Indian Ocean earthquake. *Geophysical Journal International*, *212*(2), 1331–1343. https://doi.org/10.1093/gji/ggx462

Nfomou, N., Tongwa, A. F., Ubangoh, U. R., Bekoa, A., Metuk, N. J., & Victor, H. J. (2004). The July 2002 earthquake in the Kribi region: geological context and a preliminary evaluation of seismic risk in southwestern Cameroon. *Journal of African Earth Sciences*, *40*(3), 163–172. https://doi.org/10.1016/j.jafrearsci.2004.09.002

Odeyemi, I. B. (1989). Precambrian crustal fractures as possible sites of seismic activity in Nigeria: Ifewara fault as a case example. In *Ajakaiye DE, Ojo SB, Daniyan MA and Abatan A O. Proceedings of the National Seminar on Earthquakes in Nigeria. National Technical Committee on Earthquake Phenomena, Lagos, Nigeria* (Vol. 225).

Odeyemi, I. B. (2006). The Ifewara fault in southwestern Nigeria: Its relationship with fracture zones along the Nigerian coast. *Centre for Geodesy and Geodynamics, Toro, Bauchi State*, *113*.

Ojo, A. O., Zhao, L., & Wang, X. (2019). Estimations of Sensor Misorientation for Broadband Seismic Stations in and around Africa. *Seismological Research Letters*. https://doi.org/10.1785/0220190103

Olugboji, T. M. (2020). Satellite and Aeromagnetic Data for " Solving the Mystery of Orphan Tremors Detected in West Africa on Sept 5-7,2018" [Data set]. Mendeley. https://doi.org/10.17632/W7KKG3G37D.1

Oyawoye, M. O. (1964). The geology of the Nigerian Basement Complex—a survey of our present knowledge of them. *Journal of Mining Geology and Metal*, *1*(2pp87-103), 80–91. Retrieved from https://nmgs-journal.org/wp-content/uploads/journal/published_paper/volume-1/issue-2/ztf6mXF8.pdf

Park, J., Vernon, F. L., III, & Lindberg, C. R. (1987). Frequency dependent polarization analysis of high-frequency seismograms. *Journal of Geophysical Research*, *92*(B12), 12664. https://doi.org/10.1029/JB092iB12p12664

Park, S., & Ishii, M. (2018). Near-surface compressional and shear wave speeds constrained by body-wave polarization analysis. *Geophysical Journal International*. Retrieved from https://academic.oup.com/gji/article-abstract/213/3/1559/4898037

Pérez-Díaz, L., & Eagles, G. (2014). Constraining South Atlantic growth with seafloor spreading data: South Atlantic opening. *Tectonics*, *33*(9), 1848–1873. https://doi.org/10.1002/2014TC003644

Reading, A. M., Mao, W., & Gubbins, D. (2001). Polarization filtering for automatic picking of seismic data and improved converted phase detection. *Geophysical Journal International*, *147*(1), 227–234. https://doi.org/10.1046/j.1365-246X.2001.00501.x

Ringdal, F., & Husebye, E. S. (1982). Application of arrays in the detection, location, and identification of seismic events. *Bulletin of the Seismological Society of America*, *72*(6B), S201–S224. Retrieved from https://pubs.geoscienceworld.org/ssa/bssa/article/72/6B/S201/102166/application-of-arrays-in-the-detection-location

Rost, S. (2002). Array seismology: Methods and applications. *Reviews of Geophysics* , *40*(3). https://doi.org/10.1029/2000RG000100

Rost, S., Thorne, M. S., & Garnero, E. J. (2006). Imaging Global Seismic Phase Arrivals by Stacking Array Processed Short-Period Data. *Seismological Research Letters*, *77*(6), 697–707. https://doi.org/10.1785/gssrl.77.6.697

Roult, G., Montagner, J.-P., Romanowicz, B., Cara, M., Rouland, D., Pillet, R., et al. (2010). The GEOSCOPE Program: Progress and Challenges during the Past 30 Years. *Seismological Research Letters*, *81*(3), 427–452. https://doi.org/10.1785/gssrl.81.3.427

Saar, M. O., & Manga, M. (2003). Seismicity induced by seasonal groundwater recharge at Mt. Hood, Oregon. *Earth and Planetary Science Letters*, *214*(3), 605–618. https://doi.org/10.1016/S0012-821X(03)00418-7

Sansosti, E., Berardino, P., Manunta, M., Serafino, F., & Fornaro, G. (2006). Geometrical SAR image registration. *IEEE Transactions on Geoscience and Remote Sensing: A Publication of the IEEE Geoscience and Remote Sensing Society*, *44*(10), 2861–2870. https://doi.org/10.1109/TGRS.2006.875787

Scheidegger, A. E., & Ajakaiye, D. E. (1985). Geodynamics of Nigerian shield areas. *Journal of African Earth Sciences*, *3*(4), 461–470. https://doi.org/10.1016/S0899-5362(85)80089-0

Scholz, J.-R., Barruol, G., Fontaine, F. R., Sigloch, K., Crawford, W. C., & Deen, M. (2017). Orienting ocean-bottom seismometers from P-wave and Rayleigh wave polarizations. *Geophysical Journal International*, *208*(3), 1277–1289. https://doi.org/10.1093/gji/ggw426

Schulte-Pelkum, V., Earle, P. S., & Vernon, F. L. (2004). Strong directivity of ocean-generated seismic noise. *Geochemistry, Geophysics, Geosystems*, *5*(3). Retrieved from https://agupubs.onlinelibrary.wiley.com/doi/abs/10.1029/2003GC000520

Segall, P. (2010). *Earthquake and Volcano Deformation*. Princeton University Press. Retrieved from https://play.google.com/store/books/details?id=QLumDwAAQBAJ

Segall, P., & Lu, S. (2015). Injection-induced seismicity: Poroelastic and earthquake nucleation effects. *Journal of Geophysical Research, [Solid Earth]*, *120*(7), 5082–5103. https://doi.org/10.1002/2015jb012060

Shao, X., Ma, S., Xu, C., Zhang, P., Wen, B., Tian, Y., et al. (2019). Planet Image-Based Inventorying and Machine Learning-Based Susceptibility Mapping for the Landslides Triggered by the 2018 Mw6.6 Tomakomai, Japan Earthquake. *Remote Sensing*. https://doi.org/10.3390/rs11080978

Shearer, P. M. (1994). Global seismic event detection using a matched filter on long-period seismograms. *Journal of Geophysical Research*. https://doi.org/10.1029/94JB00498

Shirzaei, M., & Bürgmann, R. (2012). Topography correlated atmospheric delay correction in radar interferometry using wavelet transforms. *Geophysical Research Letters*, *39*(1). https://doi.org/10.1029/2011gl049971

Shirzaei, M., & Bürgmann, R. (2017). Applicability of Sentinel−1 terrain observation by progressive scans multitemporal interferometry for monitoring slow ground motions in the San Francisco Bay Area. *Geophysical Research Letters*. Retrieved from https://agupubs.onlinelibrary.wiley.com/doi/abs/10.1002/2017GL072663

Shirzaei, M., & Walter, T. R. (2011). Estimating the Effect of Satellite Orbital Error Using Wavelet-Based Robust Regression Applied to InSAR Deformation Data. *IEEE Transactions on Geoscience and Remote Sensing: A Publication of the IEEE Geoscience and Remote Sensing Society*, *49*(11), 4600–4605. https://doi.org/10.1109/TGRS.2011.2143419

Shirzaei, M., Ellsworth, W. L., Tiampo, K. F., González, P. J., & Manga, M. (2016). Surface uplift and time-dependent seismic hazard due to fluid injection in eastern Texas. *Science*, *353*(6306), 1416–1419. https://doi.org/10.1126/science.aag0262

Simons, F. J., Nolet, G., Georgief, P., Babcock, J. M., Regier, L. A., & Davis, R. E. (2009). On the potential of recording earthquakes for global seismic tomography by low-cost autonomous instruments in the oceans. *Journal of Geophysical Research*, *114*(B5), 1217.

https://doi.org/10.1029/2008JB006088

Smith, R. S., & Salem, A. (2005). Imaging depth, structure, and susceptibility from magnetic data: The advanced source-parameter imaging method. *Geophysics*, *70*(4), L31–L38. https://doi.org/10.1190/1.1990219

Smith, R. S., Thurston, J. B., Dai, T.-F., & MacLeod, I. N. (2002). ISPITM—the improved source parameter imaging method. *Geophysical Prospecting*, *46*(2), 141–151. Retrieved from https://www.earthdoc.org/content/journals/10.1046/j.1365-2478.1998.00084.x

Stachnik, J. C., Sheehan, A. F., Zietlow, D. W., Yang, Z., Collins, J., & Ferris, A. (2012). Determination of New Zealand Ocean Bottom Seismometer Orientation via Rayleigh-Wave Polarization. *Seismological Research Letters*, *83*(4), 704–713. https://doi.org/10.1785/0220110128

Sykes, L. R. (1978). Intraplate seismicity, reactivation of preexisting zones of weakness, alkaline magmatism, and other tectonism postdating continental fragmentation. *Reviews of Geophysics* , *16*(4), 621–688. https://doi.org/10.1029/RG016i004p00621

Tabod, C. T., Fairhead, J. D., Stuart, G. W., Ateba, B., & Ntepe, N. (1992). Seismicity of the Cameroon Volcanic Line, 1982–1990. *Tectonophysics*, *212*(3), 303–320. https://doi.org/10.1016/0040-1951(92)90297-J

Talwani, P., & Acree, S. (1985). Pore Pressure Diffusion and the Mechanism of Reservoir-Induced Seismicity. In K. Shimazaki & W. Stuart (Eds.), *Earthquake Prediction* (pp. 947–965). Basel: Birkhäuser Basel. https://doi.org/10.1007/978-3-0348-6245-5_14

Tanaka, S., Ohtake, M., & Sato, H. (2002). Spatio-temporal variation of the tidal triggering effect on earthquake occurrence associated with the 1982 South Tonga earthquake of Mw 7.5. *Geophysical Research Letters*, *29*(16), 3–1–3–4. https://doi.org/10.1029/2002gl015386

Townend, J., & Zoback, M. D. (2000). How faulting keeps the crust strong. *Geology*, *28*(5), 399–402. https://doi.org/10.1130/0091-7613(2000)28<399:HFKTCS>2.0.CO;2

Tsai, V. C., & Ekström, G. (2007). Analysis of glacial earthquakes. *Journal of Geophysical Research*, *112*(F3), 959. https://doi.org/10.1029/2006JF000596

Tsalha, M. S., Lar, U. A., Yakubu, T. A., Kadiri, U. A., & Duncan, D. (2015). The review of the Historical and recent seismic activity in Nigeria. *IOSR J. Appl. Geol. Geophys*, *3*(1), 48–56. https://doi.org/10.9790/0990-0311456

Vidale, J. E. (1986). Complex polarization analysis of particle motion. *Bulletin of the Seismological Society of America*, *76*(5), 1393–1405. Retrieved from https://pubs.geoscienceworld.org/ssa/bssa/article-abstract/76/5/1393/118890

Wang, F., Fan, X., Yunus, A. P., Subramanian, S. S., & Huang, R. (2019). Coseismic landslides triggered by the 2018 Hokkaido, Japan (Mw 6.6), earthquake: spatial distribution, controlling factors, and possible failure mechanism. *Landslides*, (1). https://doi.org/10.1007/s10346-019-01187-7

Wang, H. F. (2001). *Theory of linear poroelasticity with applications to geomechanics and hydrogeology*. Princeton, NJ: Princeton University Press. https://doi.org/10.1515/9781400885688

Wang, R., & Kümpel, H. (2003). Poroelasticity: Efficient modeling of strongly coupled, slow deformation processes in a multilayered half−space. *Geophysics*, *68*(2), 705–717. https://doi.org/10.1190/1.1567241

Weber, R. C., Lin, P.-Y., Garnero, E. J., Williams, Q., & Lognonné, P. (2011). Seismic detection of the lunar core. *Science* , *331*(6015), 309–312. https://doi.org/10.1126/science.1199375

Wilcock, W. S. D. (2001). Tidal triggering of microearthquakes on the Juan de Fuca Ridge. *Geophysical Research Letters*, *28*(20), 3999–4002. https://doi.org/10.1029/2001gl013370

Williams, H. R., & Williams, R. A. (1977). Kimberlites and plate-tectonics in West Africa. *Nature*, *270*(5637), 507–508. Retrieved from

https://link.springer.com/content/pdf/10.1038/270507a0.pdf

Wolin, E., Stein, S., Pazzaglia, F., Meltzer, A., Kafka, A., & Berti, C. (2012). Mineral, Virginia, earthquake illustrates seismicity of a passive-aggressive margin. *Geophysical Research Letters*, *39*(2). Retrieved from https://agupubs.onlinelibrary.wiley.com/doi/abs/10.1029/2011GL050310

Wright, J. B. (1976). Fracture systems in Nigeria and initiation of fracture zones in the South Atlantic. *Tectonophysics*, *34*(3), T43–T47. https://doi.org/10.1016/0040-1951(76)90093-7

Yagüe-Martínez, N., Prats-Iraola, P., Rodríguez González, F., Brcic, R., Shau, R., Geudtner, D., et al. (2016). Interferometric Processing of Sentinel-1 TOPS Data. *IEEE Transactions on Geoscience and Remote Sensing: A Publication of the IEEE Geoscience and Remote Sensing Society*, *54*(4), 2220–2234. https://doi.org/10.1109/TGRS.2015.2497902

Yamagishi, H., & Yamazaki, F. (2018). Landslides by the 2018 Hokkaido Iburi-Tobu Earthquake on September 6. *Landslides*, *15*(12), 2521–2524. https://doi.org/10.1007/s10346-018-1092-z

Zang, C., Ni, S., & Shen, Z. (2019). Rupture Directivity Analysis of the 2018 Hokkaido Eastern Iburi Earthquake and Its Seismotectonic Implication. *Seismological Research Letters*, *90*(6), 2121–2131. https://doi.org/10.1785/0220190131

Zhai, G., Shirzaei, M., Manga, M., & Chen, X. (2019). Pore-pressure diffusion, enhanced by poroelastic stresses, controls induced seismicity in Oklahoma. *Proceedings of the National Academy of Sciences of the United States of America*, *116*(33), 16228–16233. https://doi.org/10.1073/pnas.1819225116

Zhai, G., Shirzaei, M., & Manga, M. (2021). Widespread deep seismicity in the Delaware Basin, Texas, is mainly driven by shallow wastewater injection. *Proceedings of the National Academy of Sciences of the United States of America*, *118*(20). https://doi.org/10.1073/pnas.2102338118

Zhang, S., Li, R., Wang, F., & Iio, A. (2019). Characteristics of landslides triggered by the 2018 Hokkaido Eastern Iburi earthquake, Northern Japan. *Landslides*, *16*(9), 1691–1708. https://doi.org/10.1007/s10346-019-01207-6

Zha, Y., Webb, S. C., & Menke, W. (2013). Determining the orientations of ocean bottom seismometers using ambient noise correlation: OBS ORIENTATIONS FROM AMBIENT NOISE. *Geophysical Research Letters*, *40*(14), 3585–3590. https://doi.org/10.1002/grl.50698

Figure 1.JPEG

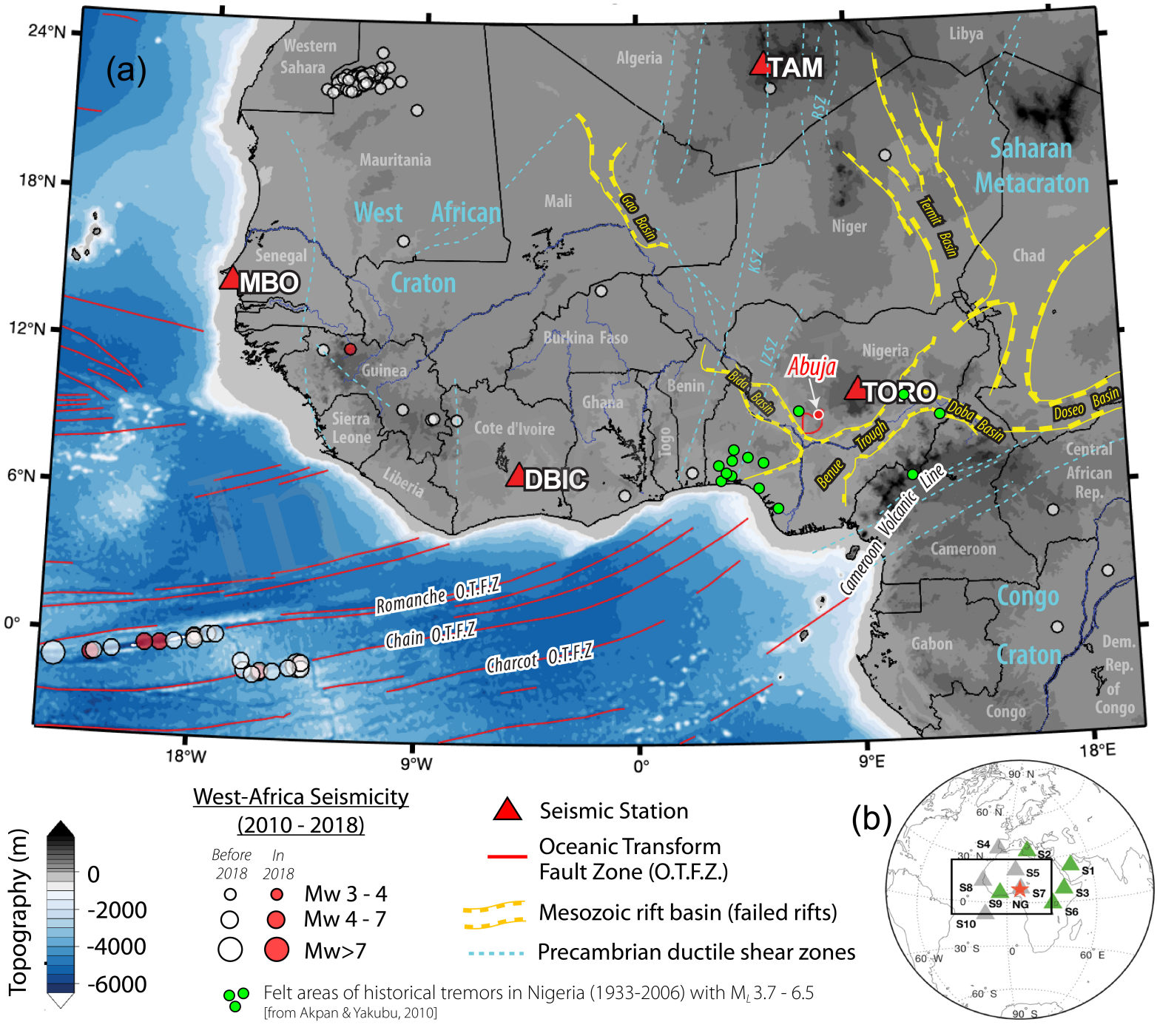

Figure 2.JPEG

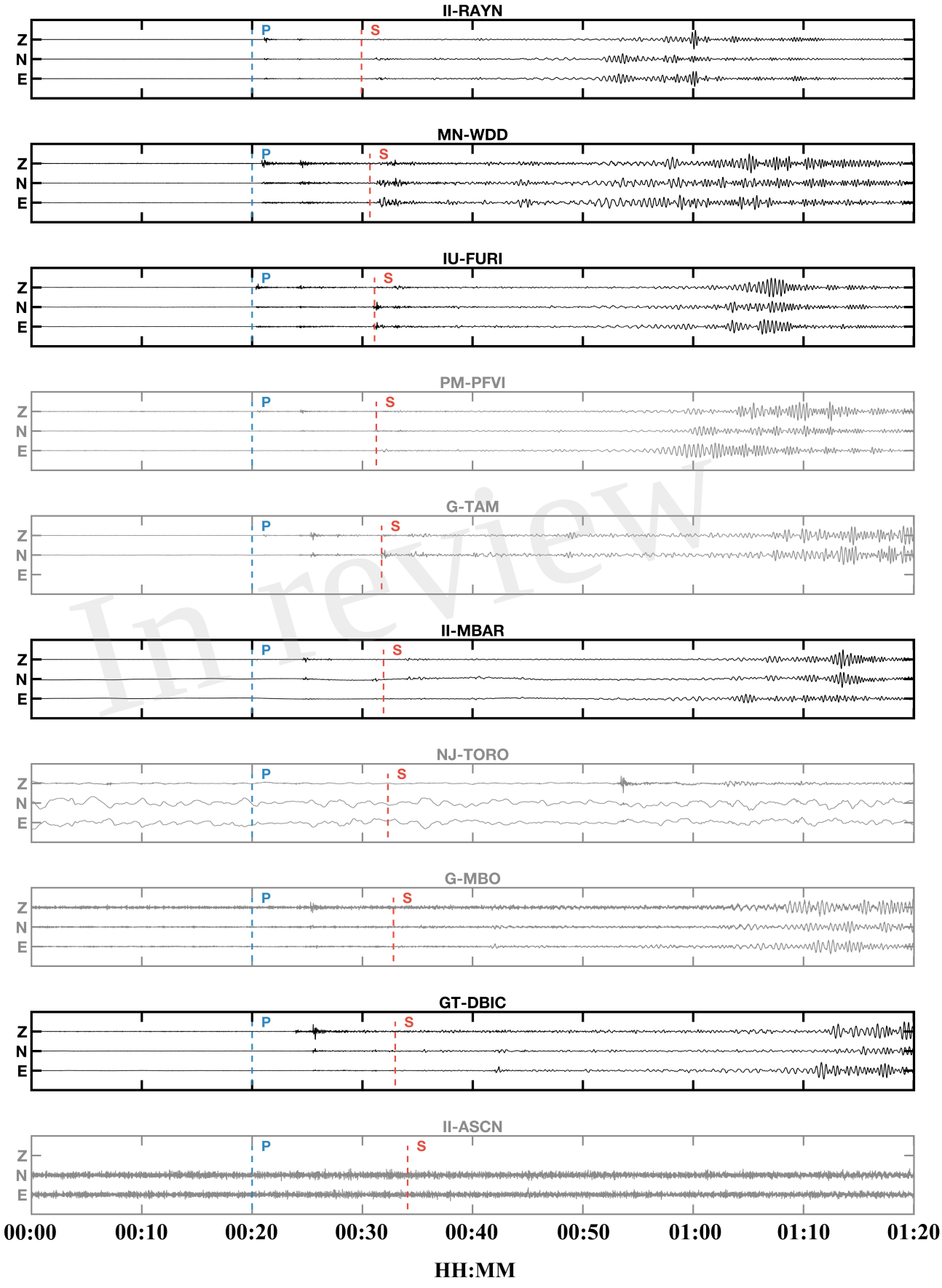

Figure 3.JPEG

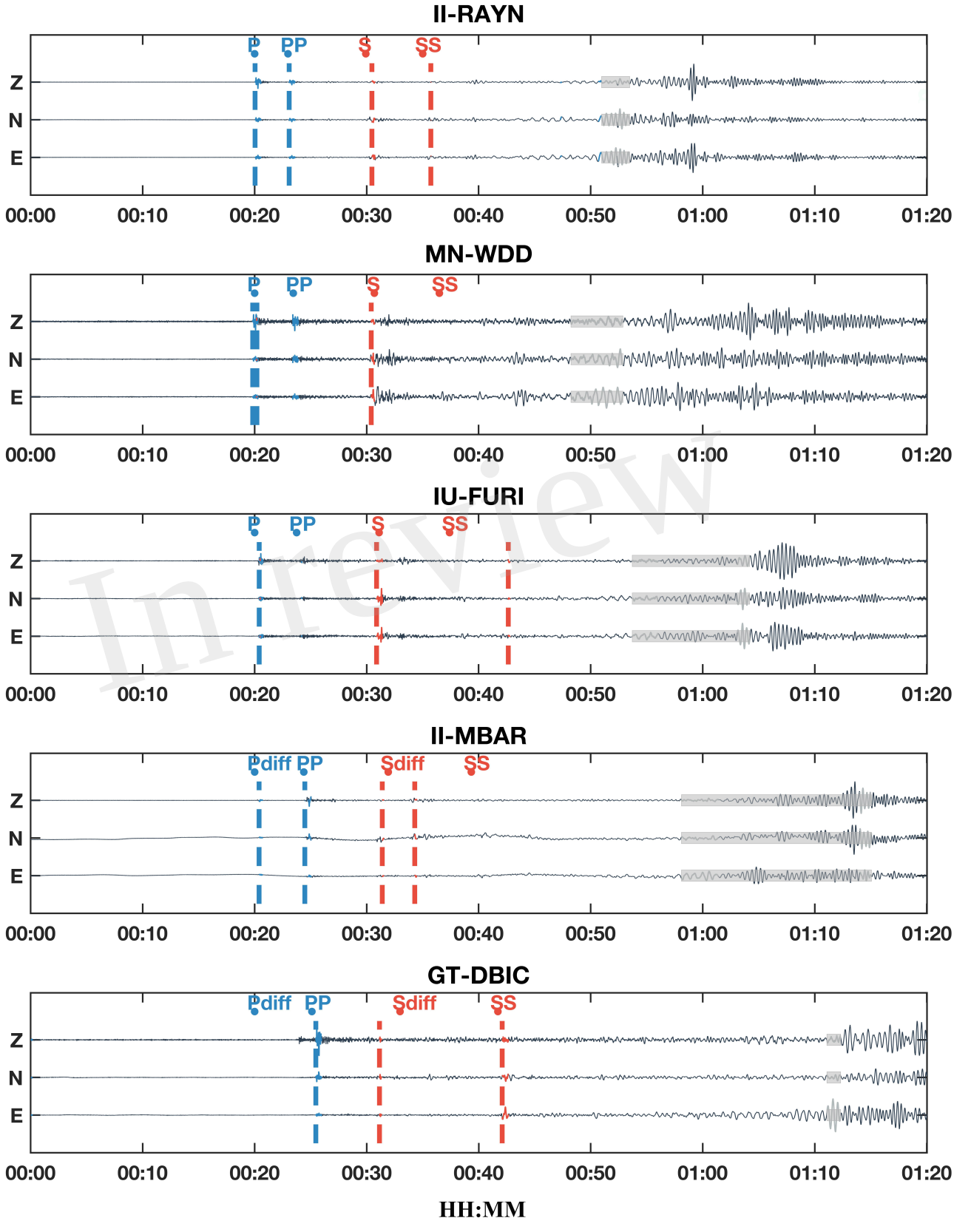

Figure 4.JPEG

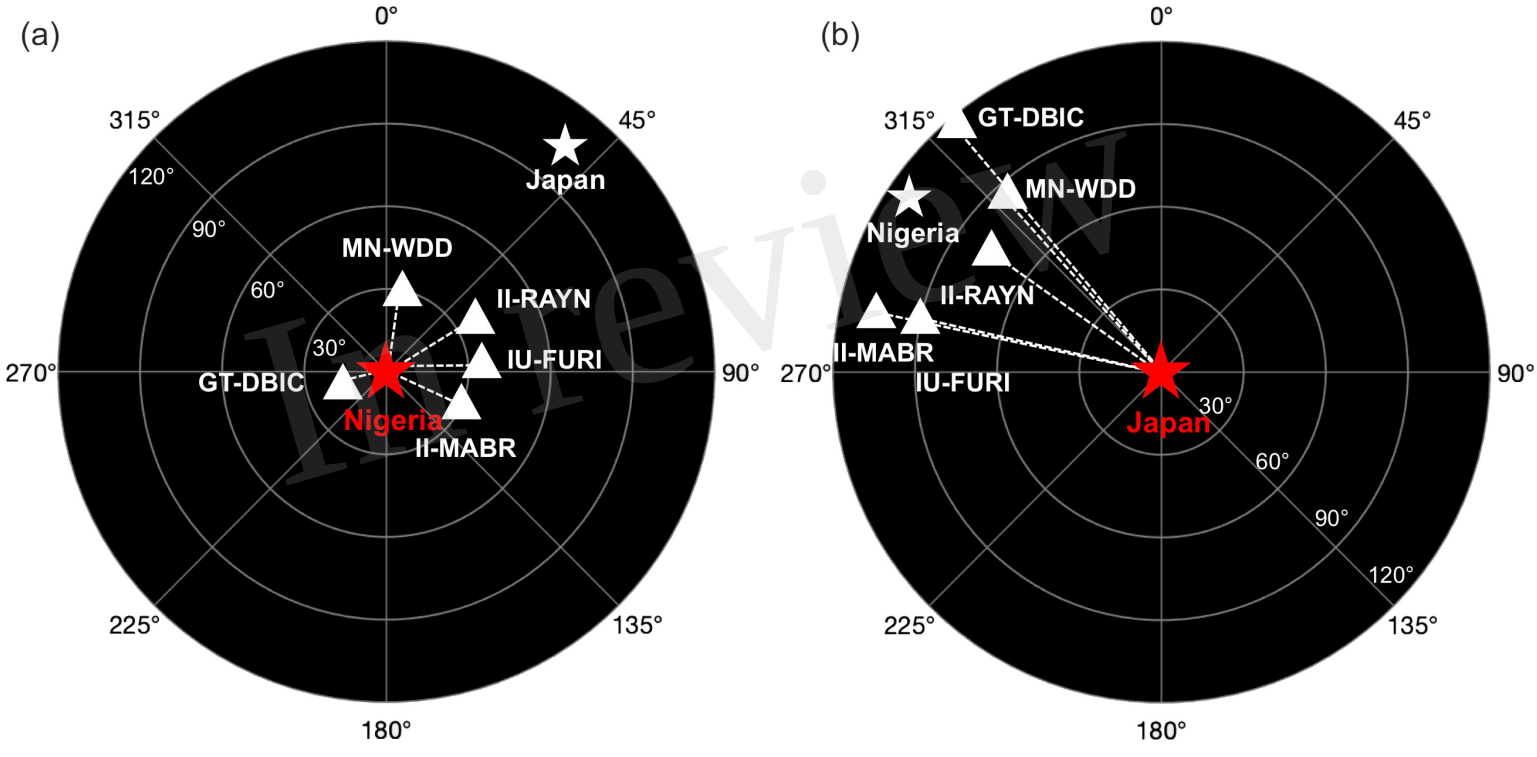

Figure 5.JPEG

Figure 6.JPEG

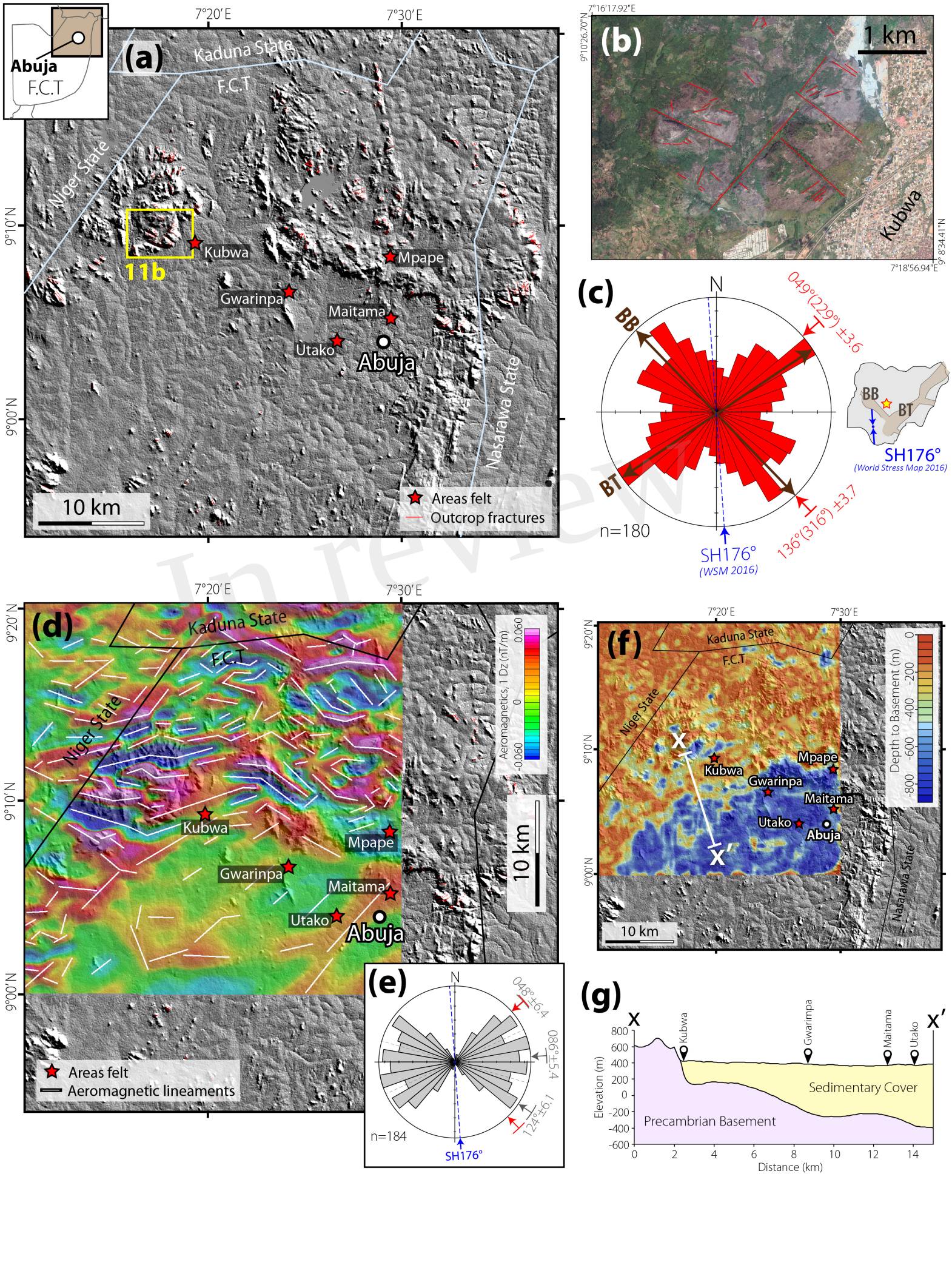

Figure 7.JPEG

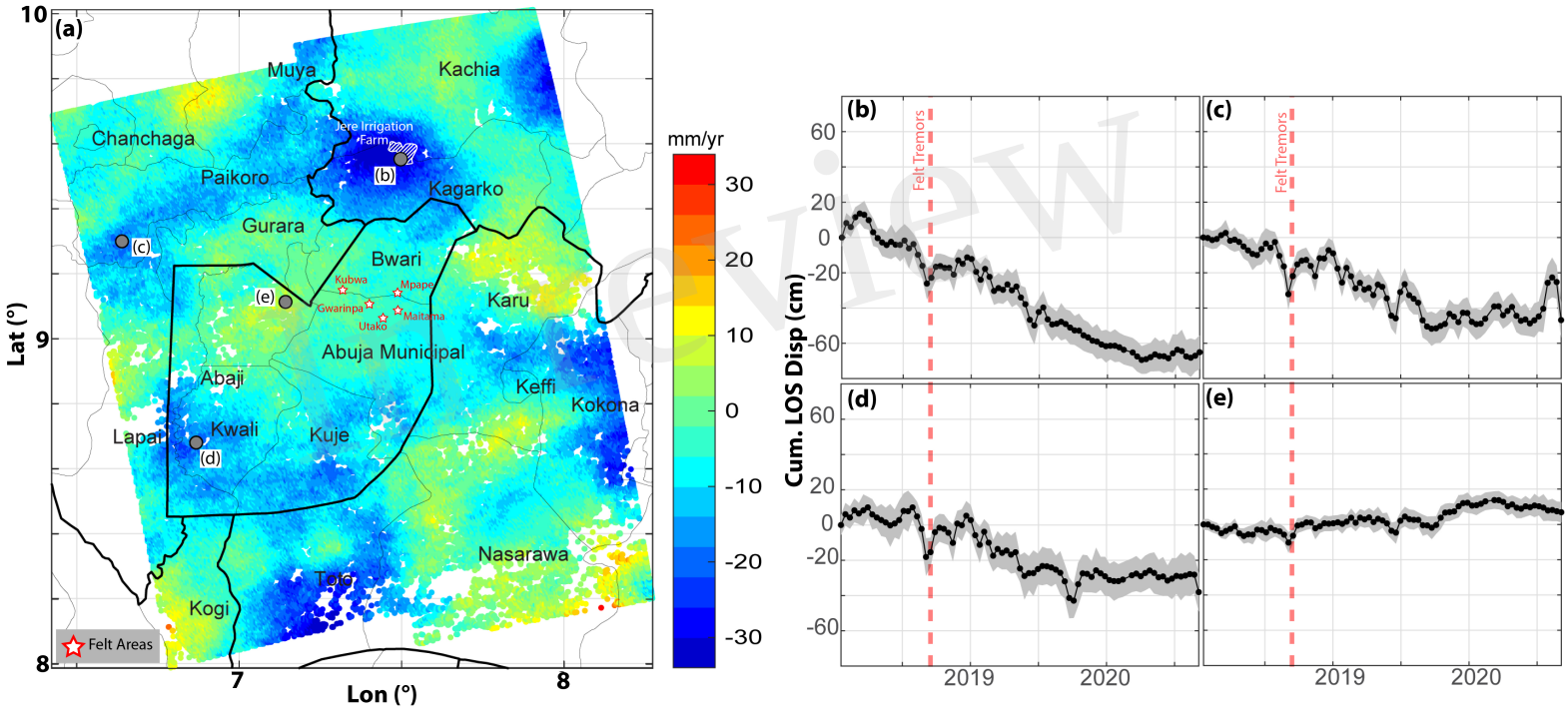

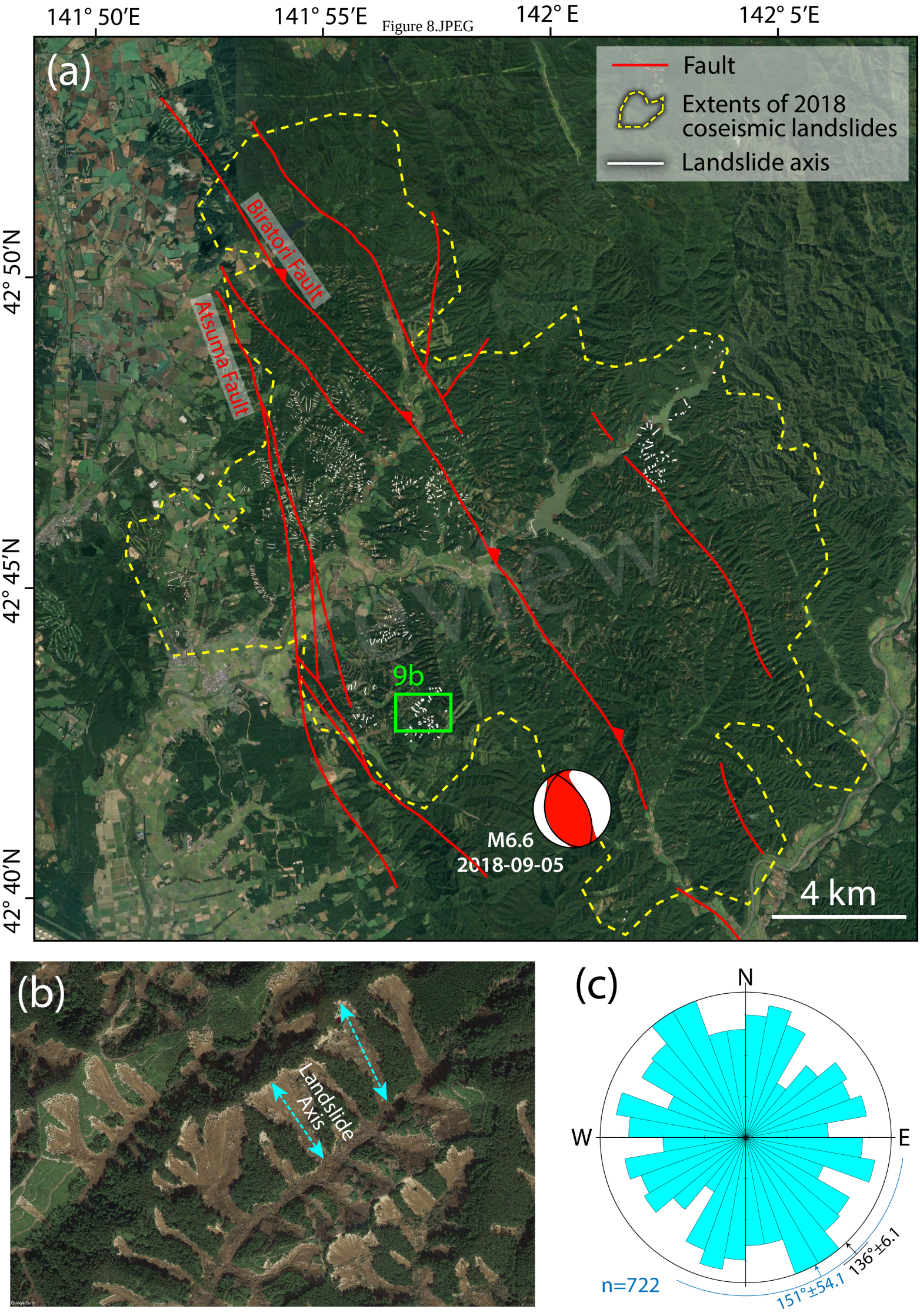
Figure 8.JPEG
141° 50′E
141° 55′E
142° E
142° 5′E
42° 50′N
42° 45′N
42° 40′N
(a)
Fault
Extents of 2018 coseismic landslides
Landslide axis
Biratori Fault
Atsuma Fault
9b
M6.6
2018-09-05
4 km
(b)
Landslide Axis
(c)
N
W
E
n=722
151°±54.1
136°±6.1